Role of tides on the formation of the Antarctic Slope Front at the Weddell-Scotia Confluence

M. M. Flexas[1,2], M. P. Schodlok[1,3], L. Padman[4], D. Menemenlis[1], and A. H. Orsi[5]

[1]Jet Propulsion Laboratory, California Institute of Technology, Science Division, Pasadena, California, USA, [2]Previously at IMEDEA, UIB-CSIC, Spain, [3]Joint Institute for Regional Earth System Science and Engineering, University of California Los Angeles, Los Angeles, California, USA, [4]Earth & Space Research, Corvallis, Oregon, USA, [5]Texas A&M University, Department of Oceanography, College Station, Texas, USA

Abstract The structure of the Antarctic Slope Front (ASF) and the associated Antarctic Slope Current (ASC) on the Scotia Sea side of the Weddell-Scotia Confluence (WSC) is described using data from a hydrographic survey and three 1 year long moorings across the continental slope. The ASC in this region flows westward along isobaths with an annual mean speed of $\sim$0.2 m s^{-1}, with time variability dominated by the K_1 and O_1 tidal diurnal constituents, a narrowband oscillation with $\sim$2-week period attributable to the spring/neap tidal cycle, and seasonal variability. Realistic and idealized high-resolution numerical simulations are used to determine the contribution of tides to the structure of the ASF and the speed of the ASC. Two simulations forced by realistic atmospheric forcing and boundary conditions integrated with and without tidal forcing show that tidal forcing is essential to reproduce the measured ASF/ASC cross-slope structure, the time variability at our moorings, and the reduced stratification within the WSC. Two idealized simulations run with tide-only forcing, one with a homogeneous ocean and the other with initial vertical stratification that is laterally homogeneous, show that tides can generate the ASC and ASF through volume flux convergence along the slope initiated by effects including the Lagrangian component of tidal rectification and mixing at the seabed and in the stratified ocean interior. Climate models that exclude the effects of tides will not correctly represent the ASF and ASC or their influence on the injection of intermediate and dense waters from the WSC to the deep ocean.

1. Introduction

The Antarctic Slope Front (ASF) [*Gill*, 1973; *Ainley and Jacobs*, 1981; *Jacobs*, 1991] is an almost circumpolar structure [*Whitworth et al.*, 1998] with strong subsurface scalar property gradients separating cold inshore waters over the Antarctic continental shelf from warm, salty Circumpolar Deep Water (CDW) offshore. Inshore waters are formed over the continental shelf by a mixture of Antarctic Surface Water (AASW), dense water contributions from winter sea ice formation, and ice shelf melting. The offshore CDW is characterized by its local subsurface potential temperature maximum θ_{max}. The cross-slope density gradient of the ASF is associated with an along-slope flow called the Antarctic Slope Current (ASC) that flows with the shallow water to the left (i.e., generally westward around Antarctica). The ASF often shows a V-shaped structure [*Gill*, 1973] with a thickened layer of AASW inside the "V."

Mixing processes at the ASF are instrumental in the ventilation (i.e., injection of surface-modified water into the deeper ocean interior) of the world ocean. Ventilation takes place through the production of Antarctic Bottom Water (AABW, defined by potential temperature $\theta > -1.85°C$ and neutral density $\gamma^n > 28.27$ kg m^{-3} [*Gill*, 1973; *Foster and Carmack*, 1976a; *Killworth*, 1977]) and less dense water masses that intrude into the Antarctic Circumpolar Current (ACC) at intermediate depths [*Carmack and Killworth*, 1978], in the form of Modified Circumpolar Deep Water (MCDW; *Whitworth et al.* [1998]). The MCDW is defined as water that is denser than γ^n at the CDW θ_{max} but cooler than CDW [see, e.g., *Whitworth et al.*, 1998, Figure 2; *Orsi and Wiederwohl*, 2009, Figure 2].

The three primary water masses (AASW, CDW, and dense shelf water, SW) that participate in forming MCDW meet at the ASF. The MCDW is formed by direct diapycnal mixing between AASW and either CDW or SW. Direct mixing between AASW and CDW can occur if the AASW is sufficiently cold, e.g., at the base of the
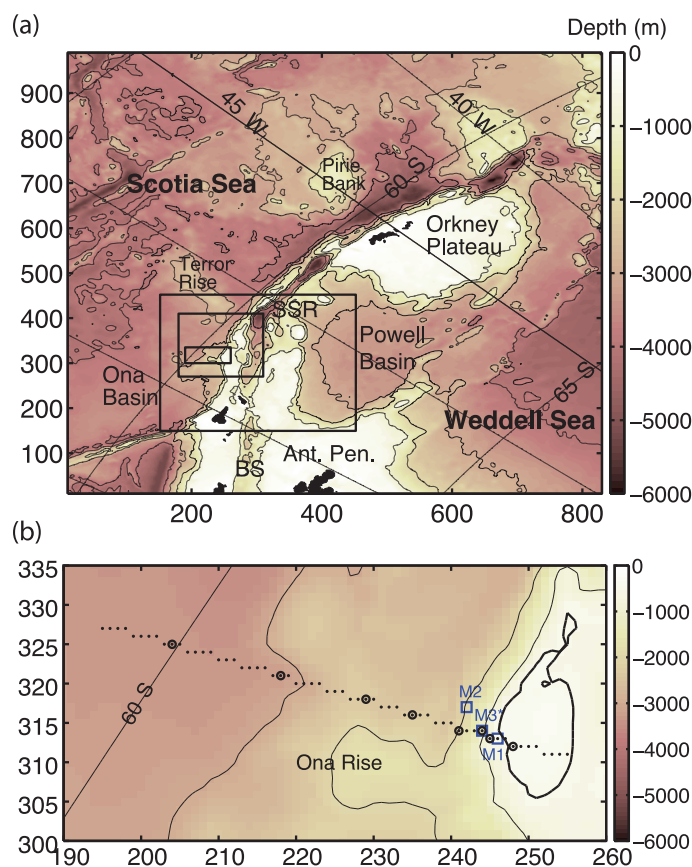
Figure 1. (a) Bathymetry of the model domain in the cube-sphere projection (~1 km grid spacing). The domain covers from 58°S to 64°S and from 40°W to 57°W. Main topographic features are indicated. The domain is centered at the western sector of the Weddell-Scotia Confluence and South Scotia Ridge (SSR), separating the Weddell Sea from the Scotia Sea, and it is bounded at its westernmost end by the tip of the Antarctic Peninsula (Ant. Pen.) and Bransfield Strait (BS). Black boxes indicate subareas used in Figures 1b, 6, 9, and 11. Black contours show 1000, 2000, 3000 and 4000 m isobaths. (b) Zoom of the area of interest. Black circles indicate approximate CTD stations. Small black dots indicate model grid nodes along the approximate hydrographic section. Blue squares indicate mooring locations for M1 at 550 m, M3* at 1100 m, and M2 at 1900 m. Black contours show 500 (thick line), 1000, 2000, and 3000 m isobaths.
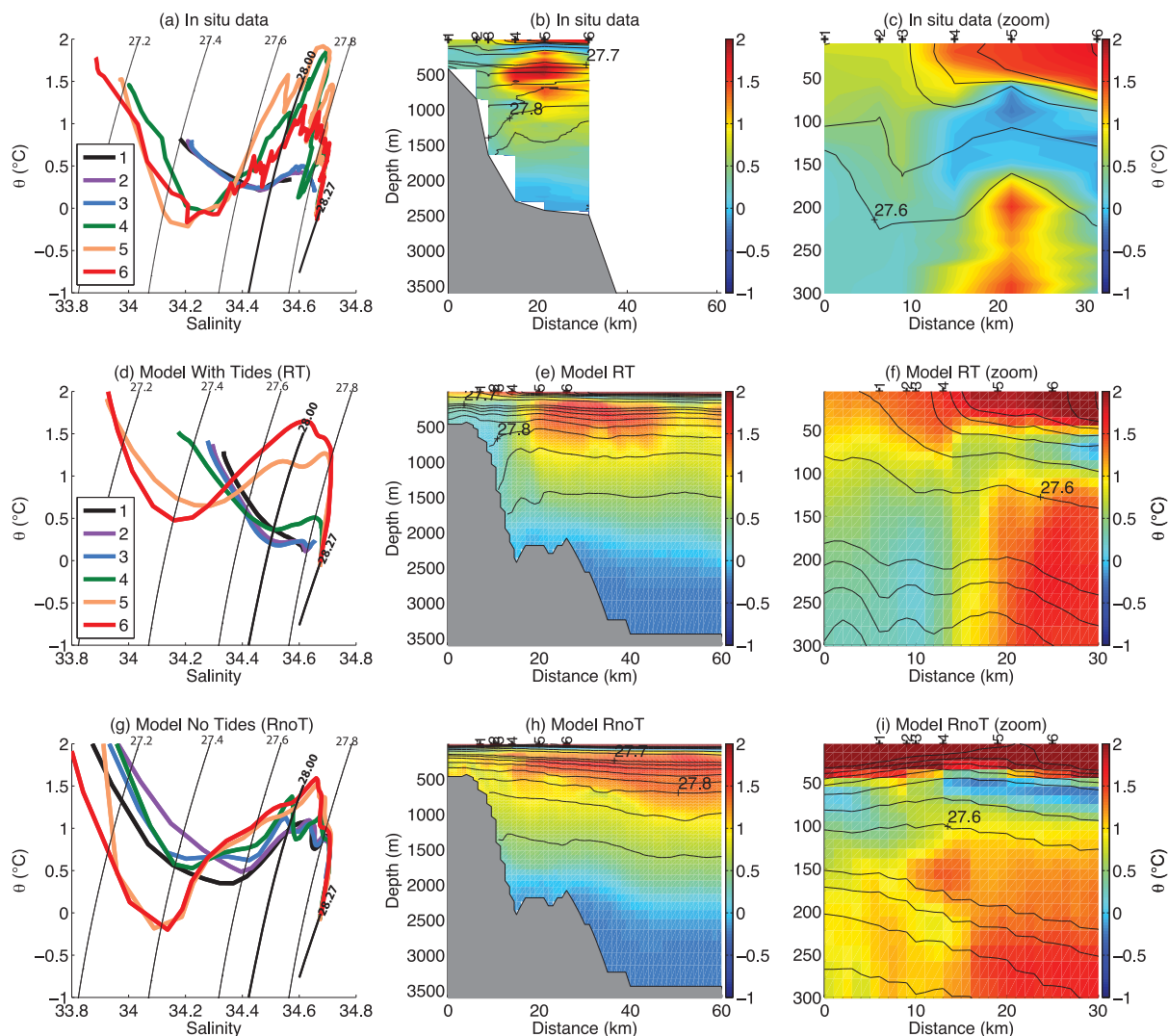
winter mixed layer after convection has cooled the AASW to near the surface freezing point of ~−1.85°C [*Whitworth et al.*, 1998; *Orsi et al.*, 2002]. Alternatively, MCDW can be formed by diapycnal mixing between AASW and SW, followed by isopycnal mixing of the product with CDW. Subsequent mixing of MCDW with SW can produce water that is sufficiently dense to flow down the continental slope as a dense water plume to contribute to AABW [*Gill*, 1973]. Lighter mixture products can spread laterally as intrusions at shallower levels where their density matches that of the ambient water [*Carmack and Killworth*, 1978].

The dynamic properties of the ASF determine the magnitude of cross-slope exchanges between the continental shelf and adjacent deep ocean. Processes that alter the mixing rates between different water masses at this junction will determine the relative contributions of shelf waters to deep ventilation by dense plumes of AABW and intermediate-depth ventilation of the ACC by eddy-driven isopycnal stirring.

In this paper, we focus on the ASF and ASC around the edges of the Weddell Scotia Confluence (WSC; *Gordon* [1967], in *Patterson and Sievers* [1980]). The WSC is a region of particularly low stratification over the continental shelf and ridges that separate the Weddell Sea from the Scotia Sea (Figure 1). The intermediate-depth layers of the Weddell Sea contain Warm Deep Water, a premodified form of CDW that has gone around the southern limb of the Weddell Gyre [*Foster and Carmack*, 1976b]. The WSC is filled with cold MCDW resulting from the mixture of WDW, CDW from the Scotia Sea, and shelf water from near the tip of the Antarctic Peninsula [*Whitworth et al.*, 1994, 1998] with contributions of meltwater from Filchner-Ronne and Larsen ice shelves [*Fahrbach et al.*, 1995; *Hellmer et al.*, 2008; *Caspel et al.*, 2015]. The ASF in this region follows the upper continental slope (~700–1000 m isobaths) from south of the tip of the Antarctic Peninsula [*Thompson and Heywood*, 2008] into the western sector of the South Scotia Ridge [*Heywood et al.*, 2004; *Palmer et al.*, 2012; *Thompson et al.*, 2014]. The ASF then continues to the northern side of the Ridge and into the Scotia Sea (Figure 2b) where a westward current over the outer shelf edge and upper slope was observed by *Nowlin and Zenk* [1988] and *Palmer et al.* [2012].

Most studies to date have considered the ASF to be a result of large-scale atmospheric forcing by wind stress combined with the contrast in hydrographic properties between offshore and shelf-resident water masses; the latter are strongly affected by surface buoyancy fluxes [*Gill*, 1973]. However, we expect that the structure of the ASF, and the strength of the associated ASC, will also depend on the mixing and advective

Figure 2. Comparison of realistic model outputs with in situ data from 1 February 2010. (a) Potential temperature (θ, °C)-salinity diagrams from in situ data. Thin black lines show potential density (σ_θ, kg m^{-3}) contours of 27.20, 27.40, 27.60, and 27.80 kg m^{-3}. Thick black lines show neutral density contours of 28.00 and 28.27 kg m^{-3}. (b) Vertical section of θ (°C) from in situ data with σ_θ isolines (drawn every 0.1 kg m^{-3} for $\sigma_\theta < 27.7$; every 0.02 kg m^{-3} for $\sigma_\theta > 27.7$) along hydrographic stations 1–6 (marked at surface; geographical location shown in Figure 1b). (c) Zoom of b, from surface to 300 m. (d, e, f) Same as before, for model simulation with tides (RT). (g, h, i) Same as before, for model simulation without tides (RnoT).

processes occurring at this complex water mass boundary. Studies of the ASF in the northwestern Ross Sea have shown that one relevant process affecting both cross-slope advection and mixing is energetic tidal currents [*Gordon et al.*, 2004, 2009; *Whitworth and Orsi*, 2006; *Muench et al.*, 2009; *Padman et al.*, 2009; *Wang et al.*, 2010; *Budillon et al.*, 2011]. Measurements from the continental slope in the WSC region also show tide-forced cross-slope advection of CDW, sufficient to move CDW onto the continental shelf on a daily basis [*Trasviña et al.*, 2011; *Palmer*, 2012], which would provide the conditions needed for direct mixing of CDW and shelf-resident water masses as reported by *Padman et al.* [2009] in their Ross Sea study. Tide models indicate that tidal currents can be of comparable magnitude to the expected mean flows along much of the continental slope around the WSC [*Padman et al.*, 2006].

Based on these observations, we hypothesize that tides play a substantial role in setting the structure of the ASF and ASC in the WSC region and the properties of water masses in the WSC. We investigate this hypothesis using current meter data from three moorings on the northern slope of the South Scotia Ridge, hydrographic profiles collected in the region during mooring deployment and recovery cruises in austral summer, and a set of high-resolution numerical simulations. The outline of the paper is as follows. In section 2, we introduce hydrographic and current measurements and outline the main

Table 1. List of Instruments and Sensors (V = Velocity; C = Conductivity; T = Temperature; P = Pressure)[a]

Mooring	H(m)	Instrument	$Z_i(m)$
2009–2010			
M1	572	VCT	277
		VCTP	375
		VCT	556
M2	1969	CTP	430
		VCTP	645
		CTP	855
		VCTP	1077
		VCTP	1296
		VCTP	1513
		VCTP	1730[+]
		VTC	1947
2012–2013			
M3*	1112	VCTP	523
		VCTP	719
		VCTP	919
		VCTP	1082

[a]Mooring M1 was located at 60.418°S, 52.950°W; M2 at 60.376°S, 52.963°W; and M3* at 60.402°S, 52.965°W. Mooring M1 was deployed on 22 February 2009 and M3* on 27 February 2009. They were both recovered on 30 January 2010. Instrument marked with symbol ([+]) stopped recording velocity on 29 September 2009. Mooring M3* was deployed on 22 January 2012 and recovered on 22 January 2013.

observations. We then present a set of numerical model simulations (section 3) that includes two realistic simulations and their comparison with in situ data, and two idealized simulations that are used to study tidal contributions to mixing and advection. Results are discussed in section 4 with conclusions in section 5.

2. Hydrographic and Current Measurements

The US-Spanish contribution to the Synoptic Antarctic Shelf-Slope Interaction study (SASSI) core project of the International Polar Year focused on the southwestern region of the Scotia Sea during two cruises in January 2008 (ESASSI-08; *Palmer* [2012]) and February 2009 (ACROSS). The main objective of the program was to study the outflow of intermediate and deep water masses from the Weddell Sea into the Scotia Sea through gaps in the western portion of the South Scotia Ridge. The program included year-long moorings and hydrographic surveys with conductivity-temperature-depth (CTD) profilers.

Two moorings (M1 and M2, Figure 1b) were deployed over the continental slope in February 2009 by the Argentinian *RV Puerto Deseado* (ACROSS cruise), and recovered 1 year later, in January 2010, by the Spanish *RV Hesperides* (ESASSI-10 cruise). The Spanish program continued for two more years, including deployment of a third mooring (M3*, Figure 1) in January 2012 by *RV Hesperides* (ELEFANTE-12 cruise). This mooring was recovered 1 year later, in January 2013, by *RV Hesperides* (ELEFANTE-13 cruise).

Mooring M1 was deployed at the shelf break at the 572 m isobath, and mooring M2 was deployed over the midslope, at the 1969 m isobath; they were ∼4 km apart. Mooring M3* was deployed over the upper slope, at the 1112 m isobath. Each mooring was equipped with several temperature, conductivity, and pressure sensors (Microcat SBE-37/39 instruments), and velocity recorders (Aanderaa RCM-7/9 and Aquadopp current meters). Sensors were separated vertically by ∼200–300 m (Table 1). Microcats were calibrated before and after deployment and no drifts were reported. The conductivity sensor located at 1947 m on Mooring M2 had an offset estimated at −0.548 salinity units using CTD data obtained during the recovery cruise. Microcat and current meter data were cleaned and preprocessed using standard procedures that included removal of spikes and linear interpolation of data gaps shorter than 6 h.

Hydrographic profiles were measured with CTDs near the mooring sites during each cruise along a section perpendicular to the continental slope (Figure 1b). Salinity measurements were calibrated onboard using a Guildline Autosal Salinometer by standardizing the internal reference against IAPSO standard seawater.

2.1. Hydrographic Properties

The hydrographic section taken on the northern side of the South Scotia Ridge in February 2010 shows the ASF as a density front over the midslope between stations #3 and #4 (700–1500 m isobaths; Figure 2b). Mooring data show time-averaged along-slope westward currents (Table 2), consistent with previous studies by *Nowlin and Zenk* [1988] and *Palmer et al.* [2012].

The separation between AASW and CDW, defined as the neutral density (γ^n) at the depth of the θ_{max} of the regional CDW offshore (see section 1), occurs at $\gamma^n = 28.00$ kg m^{-3} (potential density $\sigma_\theta \sim 27.70$ kg m^{-3}). The offshore stations #4 and #5 include CDW (Figures 2a and 2b) with a $\theta_{max} \approx 2.0$°C centered near depth $z = 500$ m, about the depth of the shelf break. Inshore stations #1 to #3 contain AASW ($\gamma^n < 28.00$ kg m^{-3}; $\sigma_\theta < 27.70$ kg m^{-3}), and MCDW ($28.00 < \gamma^n < 28.27$ kg m^{-3}; $27.70 < \sigma_\theta < 27.83$ kg m^{-3}) that is ∼1.5°C

Table 2. Mean and Standard Deviation (in Brackets) of In Situ Data (*Obs*)[a]

			Obs	RT – Obs	RnoT – Obs
M1	556	S	34.56 (0.02)	0.05 (0.03)	0.10 (0.03)
		θ	0.21 (0.28)	0.46 (0.35)	0.91 (0.34)
		σ_θ	27.74 (0.01)	0.02 (0.01)	0.03 (0.01)
		U	−19.63 (7.22)	−7.94 (9.32)	11.03 (9.38)
		V	−16.11 (5.56)	9.52 (6.78)	10.59 (6.74)
M2	645	S	34.60 (0.03)	0.04 (0.04)	0.10 (0.03)
		θ	0.22 (0.35)	0.42 (0.43)	0.82 (0.38)
		σ_θ	27.77 (0.01)	0.01 (0.01)	0.03 (0.01)
		U	−8.53 (4.67)	−5.26 (9.84)	6.53 (11.08)
		V	−5.16 (2.77)	−0.53 (4.83)	4.76 (5.28)

[a]Mean difference and standard deviation of the differences between model simulations (*RT* and *RnoT*) and in situ data. Variables: Salinity (*S*), potential temperature (θ, °C), potential density (σ_θ, kg m^{-3}), zonal (U) and meridional (V) velocity components (cm s^{-1}), at 556 m at mooring M1 and at 645 m at mooring M2, from 1 March 2009 to 1 January 2010.

cooler than the offshore CDW θ_{max} (Figure 2a). This relatively fresh, cold water is detached from the slope at a depth of about 1000 m, intruding into CDW below the depth of θ_{max} at station #4 (Figure 2b).

Offshore profiles (stations #4 to #6) have near-surface water that is fresh and warm ($S \sim 34.0$, $\theta > 1°$C) relative to inshore profiles ($S \sim 34.3$, $\theta > 0°$C). Offshore profiles show subsurface temperature minima ($\theta < 0°$C) at 100–150 m (Figures 2a and 2c) that are much more pronounced than at stations #1 to #3. These offshore profiles also contain relatively warm CDW and MCDW that is much warmer than the MCDW at the inshore stations. In general, θ, S, potential density and neutral density span much larger ranges offshore than inshore.

The CTD profiles show only summer snapshots of the hydrographic spatial variability. We assess the seasonal variability by plotting θ-S pairs measured at each sensor on moorings M1 and M2 (Figures 3a and 3b). Most sensors recorded MCDW throughout the year with values of θ ranging from −0.5°C to 1.5°C; the exception was at the uppermost sensor near $z = 277$ m on mooring M1 near the shelf break, where AASW was found throughout the year with θ ranging from −0.8°C to 1°C. At all sensors, the coldest water was observed in August–September 2009 (Figure 3b). The warm CDW ($\theta_{max} \sim 2°$C) seen in the offshore CTD profiles in summer (Figures 2a and 2b) was rarely observed at the moorings.

2.2. Tidal Currents

Power spectra of currents at each mooring are dominated by tides, with substantial additional energy at lower frequencies (e.g., Figure 4a) that might represent seasonal variability. The most energetic tidal currents are diurnal ($\sim$1 cycle per day (cpd)); substantial energy is also present in the semidiurnal band ($\sim$2 cpd). We postulate that the narrowband signal centered near $f = 0.07$ cpd is tidal in origin, since its $\sim$14 day period is close to the spring-neap cycle that results from superposition of closely spaced fundamental tidal harmonics seen as narrowband signals near 1 and 2 cpd.

To further explore the tidal contribution to measured currents, we calculated current ellipse parameters for the most energetic tidal harmonics using the "T_TIDE" Matlab toolbox [*Pawlowicz et al.*, 2002], which is based on *Foreman* [1978]. The largest tidal speeds were recorded at the continental shelf break, over the lower half of the water column in Mooring M1, by the current meters at 375 m and 556 m; see Table 1 for mooring details and Figure 4 for the spectrum at 556 m. At the 556 m instrument, semimajor axis currents (U_{maj}) for the primary diurnal tides K_1 and O_1 were $\sim$0.15 m s^{-1} and $\sim$0.13 m s^{-1}, respectively (Table 3); the primary semidiurnal tidal components (M_2, S_2, and K_2) and other significant diurnal components (Q_1 and P_1) have U_{maj} values of $\sim$ 0.02–0.03 m s^{-1}.

Over the entire water column, K_1 and O_1 currents were roughly in phase at all depths (Table 4). Values of U_{maj} for these harmonics were fairly uniform with depth at each mooring, with the exception of the deepest two current meters at mooring M2. At the shelf-break mooring M1, current ellipse orientation (*Inc*) was constant with depth and the ellipse minor axes ($U_{min}(K_1)$ and $U_{min}(O_1)$) were significant and intensified close to the seabed, implying strong cross-slope depth-dependent tidal flows. In contrast, ellipse orientations at the slope moorings M2 and M3* varied with depth, and $U_{min}(K_1)$ and $U_{min}(O_1)$ were usually <0.01 m s^{-1}. The cross-slope variability of ellipse parameters implies a complex variation of tidal flow convergence and divergence along the continental slope through a tidal cycle.

The tidal analysis shows that the fortnightly signal is dominated by the *Mf* tidal component (period of 13.66 days); at the 556 m instrument on mooring M1, the value of $U_{maj}(Mf)$ was $\sim$ 0.06 m s^{-1} (Table 3). Values of
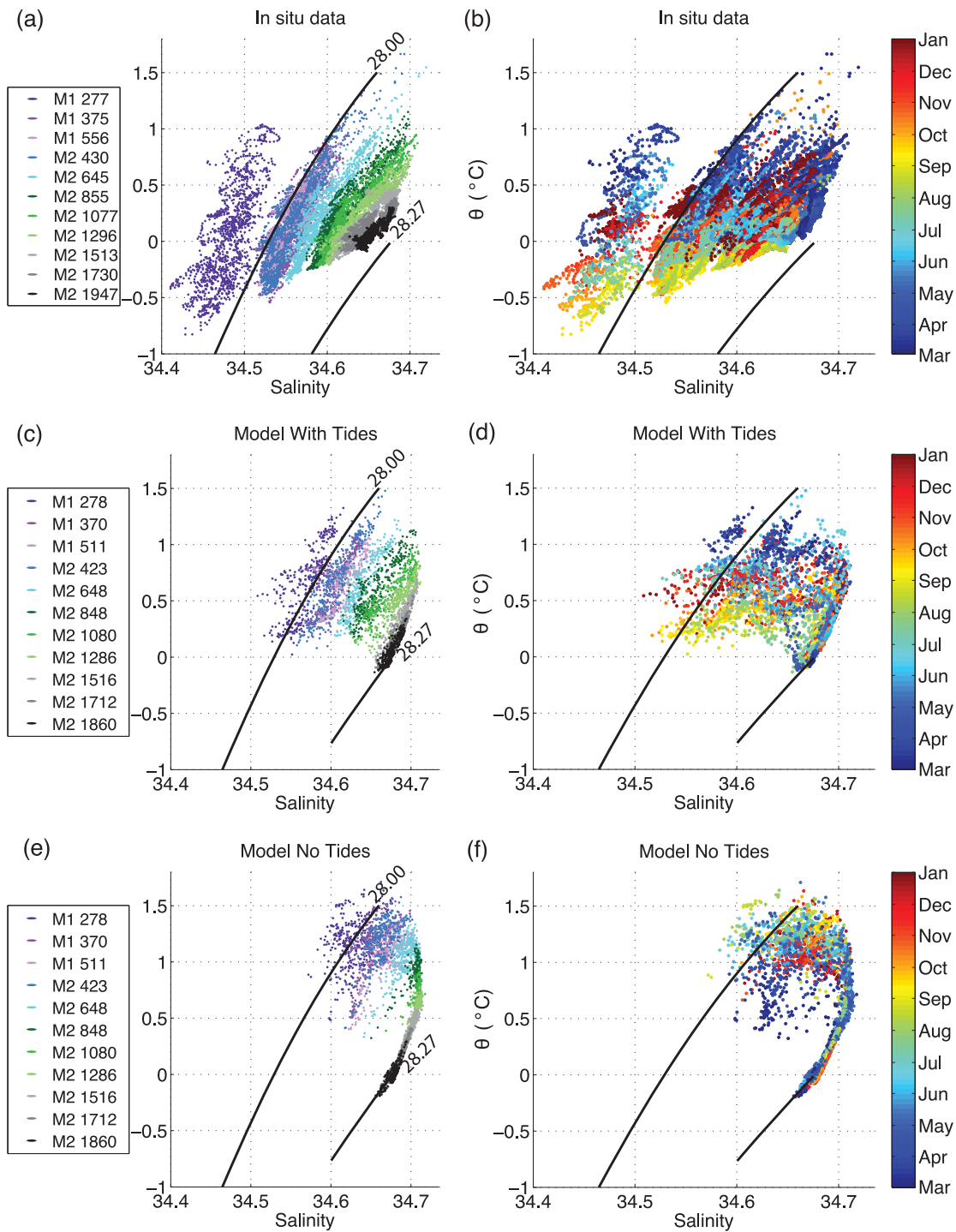
Figure 3. Comparison of realistic model outputs with in situ data from 1 March 2009 to 1 January 2010. Potential temperature (θ, °C)-salinity diagrams for (a, b) real and (c, d, e, f) virtual moorings M1 and M2 (Figure 1). (a, b) In situ data (see Table 1), filtered using a 40 h low-pass Butterworth filter. (c, d) Model simulation with tides (RT). (e, f) Model simulation without tides (RnoT). Diagrams in the left column (a, c, e) are colored by instruments and depths; diagrams in the right column (b, d, f) are colored by time. Thick black lines show neutral density contours of 28.00 and 28.27 kg m^{-3}, as in Figure 2.

$U_{maj}(Mf)$ were in the range ~0.01–0.06 m s^{-1} at all depths at all moorings (Table 5). The current ellipses for the Mf harmonic were highly elliptical (Table 5), with major axes roughly parallel to the local isobaths and no significant cross-slope component except near the seabed at the shelf-break mooring M1. Larger values
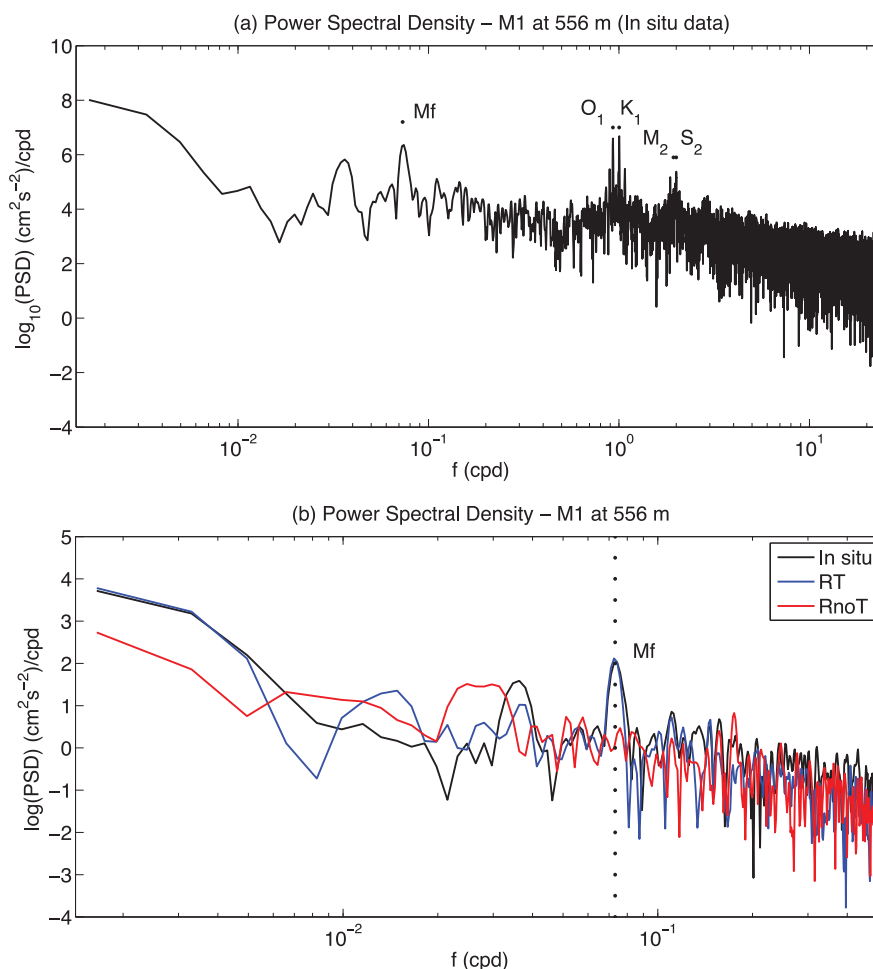
Figure 4. (a) Power spectral density (PSD) of velocity at mooring M1 in cycles per day (cpd). (b) PSD of velocity at mooring M1 at 556 m from daily averaged in situ data (black line), model simulation with tides (RT; blue line), and model simulation without tides (RnoT; red line). Note different frequency ranges for panels (a) and (b).

of $U_{maj}(Mf)$ were observed near the bottom at the shelf break (~ 0.06 m s^{-1} at the 556 m isobath, M1) and at mid depths at the upper slope (~ 0.06 m s^{-1} at a depth of 919 m in M3*). Lower velocities (~ 0.03 m s^{-1}) were found at the midslope (M2).

3. Numerical Ocean Simulations

3.1. Model Description

We used the Massachusetts Institute of Technology general circulation model (MITgcm; *Marshall et al.* [1997]), coupled to the sea ice model of *Losch et al.* [2010]. Our model domain (Figure 1a) was extracted from a conformally mapped expanded spherical cube projection [*Adcroft et al.*, 2004]. The grid consists of 840 by 1000 cells with a mean horizontal grid spacing of ~ 1 km, which is much smaller than the local Rossby radius of deformation of ~ 6–10 km. The ~ 1 km grid spacing is also required to allow adequate

Table 3. Tidal Harmonic Coefficients Obtained From the Near-Bottom (556 m) Current Meter Data at Mooring M1 Using Software "T_TIDE" [*Pawlowicz et al.*, 2002][a]

	Mf	Q_1	O_1	P_1	K_1	N_2	M_2	S_2	K_2
A (cm s^{-1})	6.2	2.9	12.6	2.8	15.1	ns	3.8	2.9	2.1
Pha (°)	19.3	217.8	205.8	238.7	212.8	ns	265.8	176.4	202.0

[a]Phase (*Pha*, °) is relative to the Greenwich meridian. Statistically insignificant results are marked (*ns*).

Table 4. Ellipse Parameters for O_1 and K_1[a]

	$H(cm)$	$Z_i(m)$	O_1				K_1			
			U_{maj}	U_{min}	Inc	Pha	U_{maj}	U_{min}	Inc	Pha
M1	572	277	9.7	2.7	71.5	200.0	12.9	4.9	72.7	206.9
		375	11.2	1.8	73.7	201.3	14.7	3.7	74.3	209.9
		556	10.3	7.2	73.8	205.8	12.4	8.6	72.7	212.8
M2	1969	645	5.3	0.3	60.0	229.6	6.3	0.7	59.8	240.3
		1077	5.7	−0.7	57.8	248.0	6.4	−0.3	59.6	262.7
		1296	5.4	−1.1	42.3	264.9	5.8	−1.0	42.7	277.7
		1513	5.3	−0.9	28.7	263.9	5.4	−0.5	27.3	280.1
		1730	3.8	0.3	29.2	255.4	3.7	0.5	26.5	264.4
		1947	2.0	−0.4	168.2	35.9	2.1	−0.5	162.6	50.0
M3*	1112	523	5.9	1.5	66.0	202.1	7.9	2.7	65.9	210.3
		719	5.6	0.9	57.2	197.7	7.2	1.1	59.6	218.3
		919	7.0	0.0	43.7	199.6	8.8	0.0	43.7	225.8
		1082	6.4	−0.1	33.5	200.0	7.2	0.0	31.4	226.8

[a]Major and minor axis ellipse (U_{maj} and U_{min}, cm s^{-1}), inclination (Inc, °), and phase (Pha, °).

resolution of steep bottom topography where slopes can exceed 0.3, e.g., between moorings M1 and M2 (Figure 1a). The vertical discretization uses 80 levels with thickness exponentially increasing with depth from ∼5 m at the surface to ∼30 m at 500 m and ∼80 m at 2000 m. Such relatively high horizontal and vertical resolution enables us to resolve the small-scale shelf-slope dynamical processes associated with the complex and often extremely steep bathymetry of the South Scotia Ridge.

Our model configuration choices, summarized in Table 6, include a flux-limited, seventh-order, monotonicity-preserving advection scheme [*Daru and Tenaud*, 2004] and the modified Leith scheme of *Fox-Kemper and Menemenlis* [2008] for horizontal viscosity. Vertical viscosity and diffusivity are parameterized according to the K-profile parameterization (KPP) [*Large et al.*, 1994]. Bottom drag is quadratic (drag coefficient, $C_D = 2.1 \cdot 10^{-3}$) and side drag is free slip. Partial cells [*Adcroft et al.*, 1997] are used to represent the sloping sea floor in our z-level vertical discretization. Bathymetry is a composite from Global Topography v14.1, updated from *Smith and Sandwell* [1997], and IBCSO Southern Ocean Bathymetry v1.0 south of 60°S [*Arndt et al.*, 2013].

We performed two realistic model runs, one with tidal forcing (hereafter RT) and one without tidal forcing (hereafter RnoT). For both runs, initial and lateral boundary conditions were obtained from a 2009–2011 adjoint-method-based optimization from the project "Estimating the Circulation and Climate of the Ocean, Phase II (ECCO2)" [*Menemenlis et al.*, 2008]. Specified fields include: ocean temperature, salinity, and horizontal velocity; sea ice thickness, concentration, salinity, and velocity; and snow thickness. Surface forcing fields were obtained from the ERA-Interim atmospheric reanalysis [*Simmons et al.*, 2007]. For RT, we added tidal forcing as barotropic horizontal velocities specified at the boundaries. Tidal velocities were obtained from the data-assimilative barotropic tidal model CATS2008b, which is a high-resolution updated version of the model described by *Padman et al.* [2002]. We included the eight most energetic primary tidal harmonics (four semidiurnals M_2, S_2, N_2, K_2, and four diurnals K_1, O_1, P_1, Q_1). Both RT and RnoT were run for years 2009 and 2010 with daily averaged output.

We also ran two idealized model configurations, one with a stratified ocean (denoted I2K1) and the other

Table 5. Ellipse Parameters for Fortnightly Variability (∼13.66 Day Period, ∼ Mf Tide)[a]

	$H(m)$	$Z_i(m)$	U_{maj}	U_{min}	Inc	Pha
M1	572	277	2.8	−0.6	42.7	27.2
		375	4.1	0.1	48.9	38.7
		556	5.7	2.4	15.0	19.3
M2	1969	645	3.2	0.0	27.1	86.3
		1077	3.9	−0.1	32.4	96.6
		1296	3.6	0.0	24.2	87.2
		1513	2.8	−0.4	20.0	63.2
		1730	1.3	−0.2	32.5	45.4
		1947	ns	ns	ns	ns
M3*	1112	523	4.2	−0.2	26.3	36.0
		719	4.9	0.1	31.5	40.7
		919	5.8	−0.2	25.0	39.7
		1082	4.1	−0.4	21.5	27.9

[a]Major and minor axis ellipse (U_{maj} and U_{min}, cm s^{-1}), inclination (Inc, °), and phase relative to the Greenwich meridian (Pha, °).

Table 6. Model Parameters and Constants

Parameter	Reference, Value
Equation of state	*Jackett and McDougall* [1995]
Advection scheme	*Daru and Tenaud* [2004]
Vertical viscosity	*Large et al.* [1994]
Horizontal viscosity	*Fox-Kemper and Menemenlis* [2008]
Vertical diffusivity	*Large et al.* [1994]
Quadratic bottom-drag	$2.1 \cdot 10^{-3}$
Side-drag	Free-slip

with a homogeneous ocean (H2K1). For I2K1, we used laterally homogeneous initial conditions with a linearly stratified vertical profile of $\theta(z) = 1.4\text{-}2 \cdot 10^{-4} \cdot z$ and constant $S = 34.7$. For H2K1, $\theta = 1^\circ$C and $S = 34.7$. For these runs, no atmospheric forcing was used, and the only external forcing was twice the amplitude of the single harmonic tidal component K_1 to approximately represent permanent spring tide with an easily diagnosed sinusoidal forcing [*Padman et al.*, 2009; *Wang et al.*, 2010]. These two model configurations were run for 28 days with daily averaged output. Additionally, I2K1 was run for the first 10 days with hourly output, and H2K1 for days 27 and 28 with hourly output.

3.2. Comparison of Realistic Simulations With Observations

The modeled mean values of θ, S, and σ_θ at locations of moored sensors are, in general, higher than the measured values for both RT and RnoT; however, the errors in RT are about half of those for RnoT (Table 2). Simulation RT also reproduces the measured cross-slope variability of $\theta(z)$ and $\theta(S)$ reasonably well (Figure 2). This simulation captures the difference in surface values of θ and S between the inshore stations within the WSC (stations #1 to #3) and the offshore stations #5 and #6, and the presence of the subsurface front (the ASF) represented by isopycnals that sink toward the continental slope below the depth of the shelf break. In contrast, RnoT fails to show substantial differences in surface properties between inshore and offshore regions, and does not generate the subsurface ASF.

Simulation RT also produces time variability of θ and S through the annual cycle that is more realistic than in RnoT (Figure 3). There are, however, large differences between the modeled values of time-dependent (S, θ) and measured values, even for RT. Measurements show colder temperatures than in RT, and the simulation fails to capture most of the AASW that is observed by the uppermost Microcat at 277 m depth on mooring M1.

Simulation RT also better reproduces the low-frequency ($f < 0.5$ cpd) variability of currents over the outer continental shelf at Mooring M1, based on power spectra (Figure 4b). This simulation generates a pronounced spectral peak with $f \sim 0.07$ cpd ($\sim$2 week period) that is almost identical to the measured value, even though the tidal forcing only includes the fundamental diurnal and semidiurnal tides ($\sim$1 and $\sim$2 cph, respectively). The addition of tides generates a stronger annual-averaged westward flow near the mooring sites (Figure 5), consistent with the frontal structure visible as downward bending of isopycnals toward the slope below the depth of the shelf break (Figure 5a). In contrast, in simulation RnoT, isopycnals are almost flat (Figure 5b).
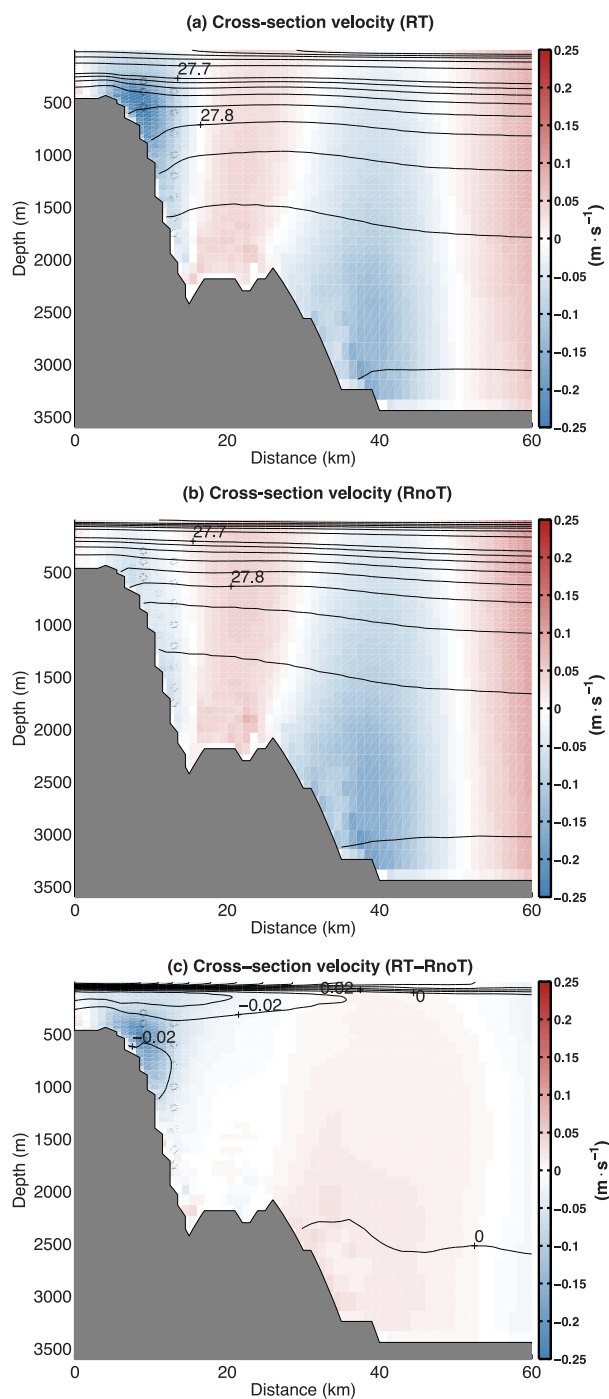
While the evaluation of modeled currents is limited to mean values (Table 2) and spectral densities for $f < 0.5$ cpd (e.g., Figure 4b) at the moorings, these comparisons suggest that including tides is required to explain the spatial and temporal variability of *subtidal* currents throughout the model domain. The maximum depth-averaged annual-mean currents in RT are about 0.5–0.6 m s^{-1} in Ona Basin and over bottom topography features such as Ona Rise, Terror Rise, and Pirie Bank (Figure 6a; see Figure 1 for locations of geographical features). Removing the effect of tides generally reduces these currents, with maximum values of $\sim$0.4 m s^{-1} (Figure 6b). The effect of tides on mean currents is most pronounced over the continental slope between the 500 and 1000 m isobaths (Figure 6c).

3.3. Tide-Forced Mixing and Advection in Idealized Model Configurations

We use our idealized simulations I2K1 and H2K1 (section 3.1), with tide forcing only, to isolate some of the processes by which tides cause differences in stratification and circulation between the realistic simulations RnoT and RT. The Ross Sea studies cited earlier point to diapycnal mixing and tidal rectification as key components of tidal impacts on water mass modification along the outer continental shelf and slope. We use the stratified simulation I2K1 to investigate the possible role of mixing, and the homogeneous simulation H2K1 to determine whether the overall response to rectification and benthic friction can lead to topographically constrained mean flows that could contribute substantially to the ASC measured at our moorings.

In the stratified idealized simulation I2K1, after 28 days of integration, a daily-averaged cross-slope vertical section of σ_θ (Figure 7) shows isopycnals below the depth of the shelf break ($\sim$600 m) bending downward toward

Figure 5. Annual mean (time-average over year 2009) cross-section velocity (m s^{-1}) from (a) simulation RT and (b) simulation RnoT along section shown in Figure 1. Black contours are potential density isolines (σ_θ, drawn every 0.1 kg m^{-3} for $\sigma_\theta < 27.7$; every 0.02 kg m^{-3} for $\sigma_\theta > 27.7$). (c) Difference between RT minus RnoT. Potential density anomalies are drawn every 0.02 kg m^{-3}.

the continental slope. Above this depth, isopycnals bend upward toward the continental shelf. The shape of the front is qualitatively similar to that observed in the annual time-averaged cross-slope vertical section obtained from the fully forced model output with tides (compare Figure 5a (RT) with Figure 7b (I2K1)). Near the surface (upper 100 m), offshore water is lighter than water over the continental shelf and slope (Figure 8c), qualitatively similar to observed distributions of AASW and results from the realistic simulation RT (Figure 2c and 2f).

As expected, the map of depth-averaged tidal current speed evaluated with this simulation (Figure 8a) is similar to the map of the major axis of the tidal component K_1 from the data-assimilative barotropic tidal model CATS2008b (Figure 8b). In a section of daily averaged currents and σ_θ taken across the South Scotia Ridge (Figure 8c; transect location shown in Figure 8a), the along-slope current flows eastward along the southern side of the South Scotia Ridge, westward on the southern side of the South Scotia Ridge trough, then eastward on the northern side of the trough. The current then turns westward again on the northern side of the ridge in the southern Scotia Sea near the location of our moorings and CTD transect. Maximum mean currents reach ∼ 0.50 m s^{-1}. This flow pattern is similar to that depicted from observational studies [*Heywood et al.*, 2004; *Palmer et al.*, 2012; *Thompson et al.*, 2014].

Substantial anomalies in depth-averaged θ over the western sector of the South Scotia Ridge are generated in this idealized model configuration with tide-only forcing (Figure 8d). In particular, values are reduced by ∼0.1-0.3°C over the continental shelf after 28 days of model integration. Since simulation I2K1 does not include atmospheric forcing and purely vertical mixing would preserve the depth-averaged value of θ, this modeled cooling must arise from cross-slope lateral transport of warm upper ocean waters off the continental shelf with replacement by onshore transport of cooler waters from below the depth of the shelf break.

In the I2K1 simulation, the time-averaged barotropic velocity at mooring M3* is ∼0.25 m s^{-1} directed along-slope towards the southwest (Figure 9a). The barotropic velocity vector rotates anticlockwise during a K_1 cycle, with the combination of mean and tidal flows leading to current speeds varying between ∼0
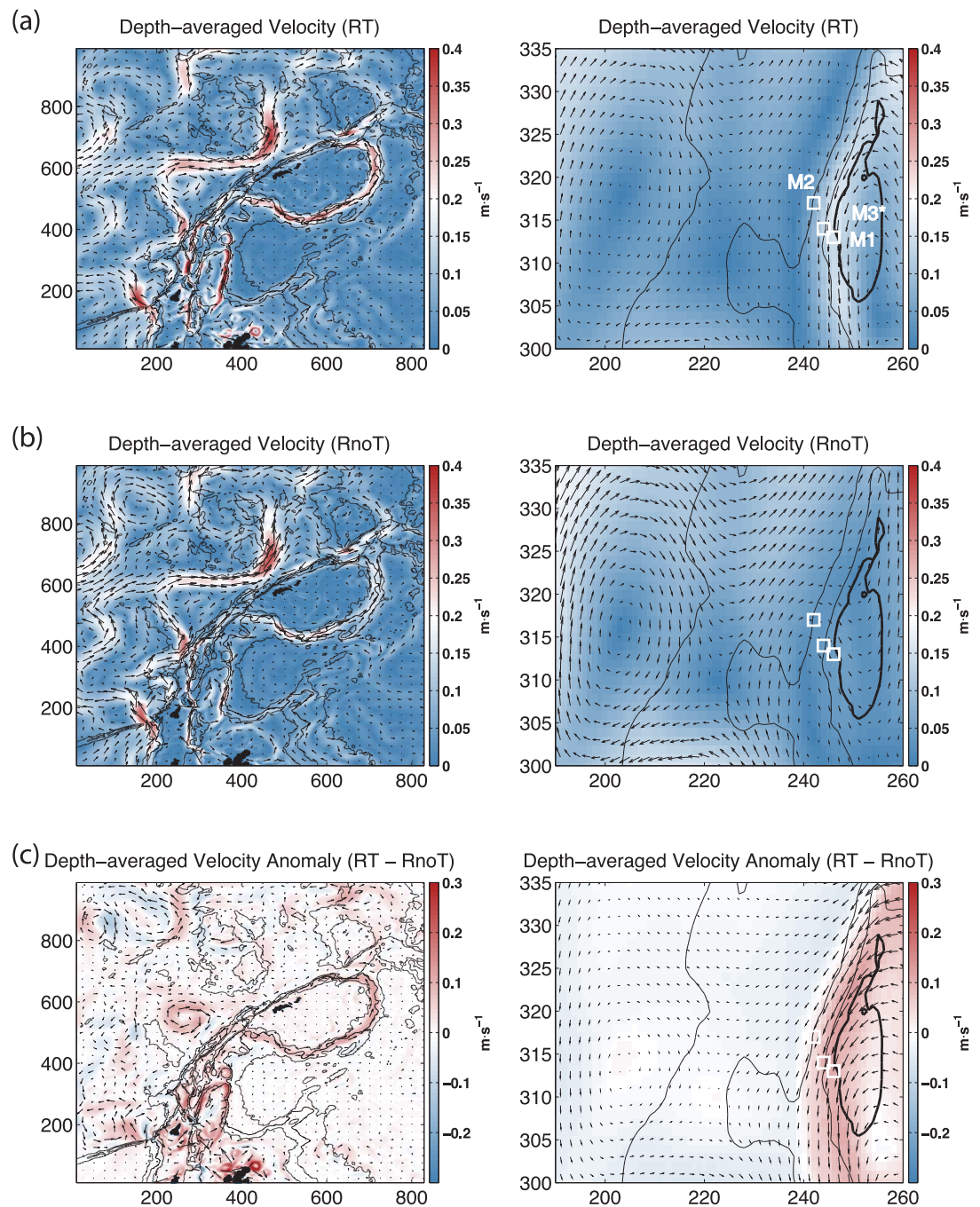
Figure 6. Annual mean (time-average over year 2009) depth-averaged velocity (m s^{-1}) from model simulation (a) with tides (RT), (b) without tides (RnoT), and (c) difference between RT minus RnoT. Black contours show 1000, 2000, and 3000-m isobaths. Right plots also show 500 m isobath (thick black contour). Note that, for clarity purposes, in left (right) plots only 1:25 (1:2) vectors are plotted.

and ∼0.5 m s^{-1}. The weakest flow occurs near flood tide while the strongest flow is near ebb tide and is directed along-slope toward the southwest. Velocities near the seabed are much smaller than the depth-averaged value. Velocity vectors throughout the water column include an offshore component from flood (hour 147) to ebb (hour 159), and an onshore component from ebb to flood (hours 159–171) (Figure 9a). A V-shape front develops from flood to ebb, and it is fully developed at ebb (Figure 9c). Observations obtained at the shelf break, from a time series of CTD profiles repeated every hour for 12 h at 61.25°S, 51.22°W (∼ $(x, y) = (370, 300)$ km in Figure 1), suggest a 12 h cross-slope motion of the warm core of MCDW
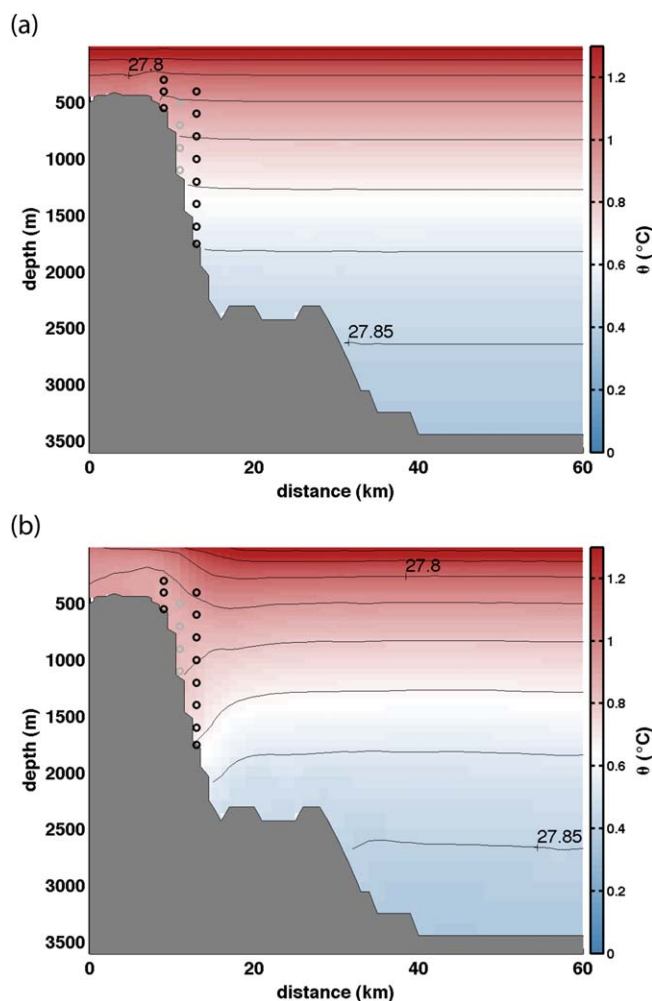
Figure 7. Idealized stratified ocean (experiment I2K1). Daily averaged potential temperature (θ, °C) snapshots for (a) day 1 and (b) day 28 along section shown in Figure 1b. Potential density isolines (in black) are drawn every 0.01 kg m^{-3}.
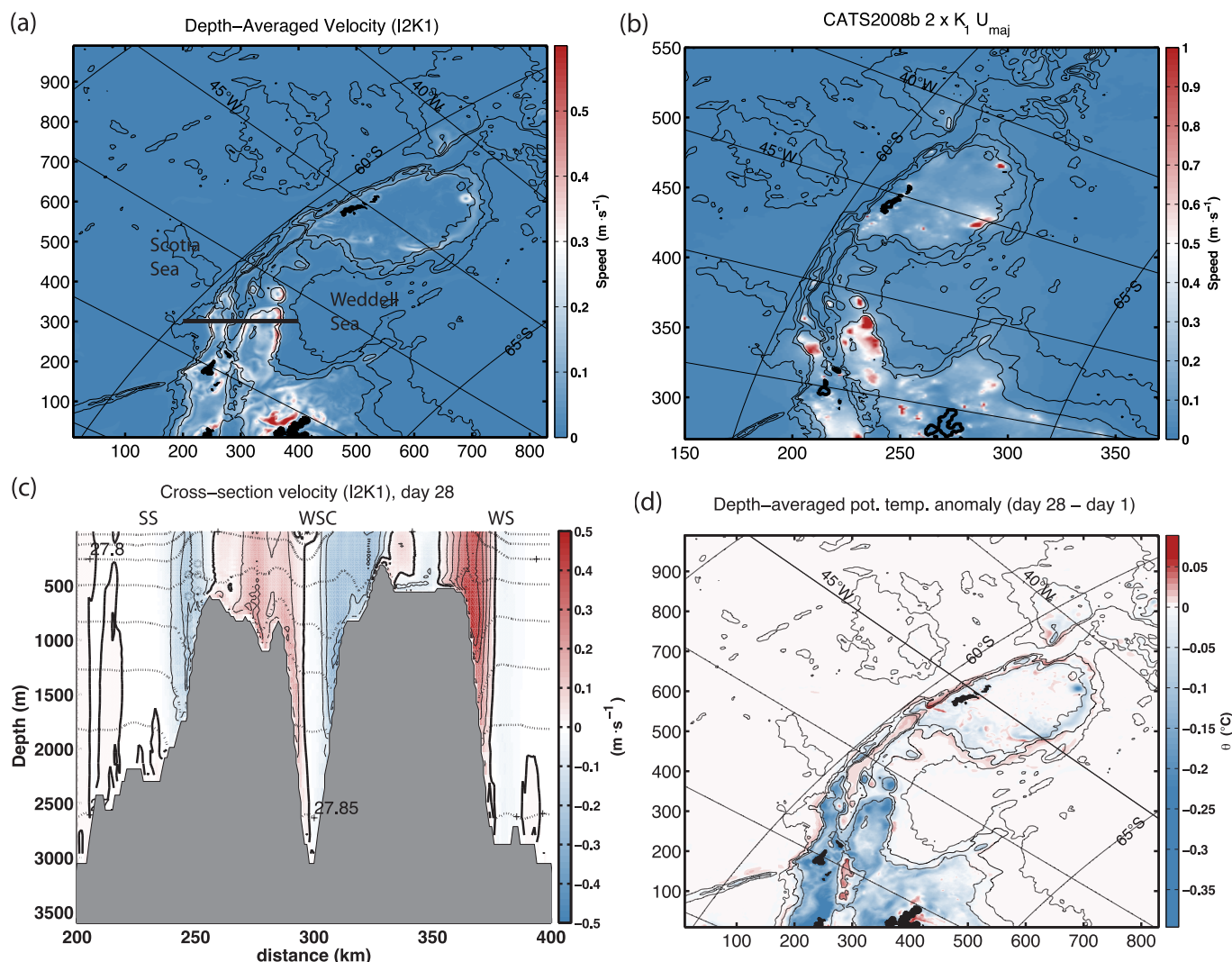
onto the shelf [*Palmer*, 2012], consistent with the cross-slope tidal currents reported here. Similar observations were reported for the northwest Ross Sea [*Whitworth and Orsi*, 2006] and tidal cross-slope advection was reproduced by a numerical model of the same region [*Padman et al.*, 2009].

Diapycnal mixing in all of our simulations is evaluated from the KPP scheme, which defines diapycnal diffusivity and viscosity below the surface boundary layer as functions of the local gradient Richardson number Ri_g, given by

$$Ri_g = \frac{N^2}{\left(\frac{\partial U}{\partial z}\right)^2 + \left(\frac{\partial V}{\partial z}\right)^2}, \qquad (1)$$

where $N(t, \mathbf{x})$ is the local buoyancy frequency, and $U(t, \mathbf{x})$ and $V(t, \mathbf{x})$ are the orthogonal horizontal velocity components of the flow. We examine the temporal variability of stratification, vertical shear, and Ri_g at two mooring sites: M1 over the shelf break; and M3* over the upper slope (Figure 10).

From flood (hour 147) to ebb (hour 159) tide, velocity has an offshore component (Figures 9a and 10a). Cold, dense shelf water moves offshore toward the slope (Figure 10b), stratification (N^2) reduces (Figure 10c), and horizontal velocities show strong vertical shear over the entire water column

(Figure 10d). At ebb (hour 159), the water column is almost homogeneous except for a thin stratified layer near the sea surface (Figure 10c), and strong vertical shear is observed near the bottom of the continental shelf (Figure 10d). From ebb to flood (hour 159–171), cold, dense subsurface offshore water is pushed back onto the continental shelf (Figure 10b), increasing stratification of the water column (flood at hour 171; Figure 10c).

The combination of stratification and shear leads to values of Ri_g (equation (1)) that are frequently less than one (Figure 10e), indicating potential for strong turbulence and mixing. In general, however, the strongest mixing occurs when the water is almost unstratified so that water mass conversion, represented in I2K1 by turbulent heat flux (Figure 10f), is generally small near the moorings, of order 1 W m^{-2}. These results suggest that diapycnal mixing might only partially explain the modeled changes in depth-averaged maps of θ for simulation I2K1 (Figure 8d), implicating advection as the primary contributor to the development of hydrographic lateral gradients in this model configuration.

We test this hypothesis by further simplifying the idealized model configuration to consist of a homogeneous ocean (simulation H2K1) in which no water mass transformation can occur. This simulation develops daily-averaged sea-level anomaly and depth-averaged flow fields that reach steady-state at about day 28 (Figure 11). As expected, the mean flow follows gradients of the time-averaged sea surface height anomaly field, which are strongest along the shelf break and upper slope. The mean flow field shows an along-slope flow from the Weddell Sea ($\sim$ 0.3 m s^{-1}) into the Scotia Sea ($\sim$ 0.1 m s^{-1}) (Figure 11d).

Figure 8. (a) Time mean (time averaged over 28 days) depth-averaged velocity (m s^{-1}) from run I2K1. (b) Speed along the major axis of 2xK_1 (U_{maj}) from data-assimilative barotropic tidal model CATS2008b. (c) Cross-section velocity (m s^{-1}; in color) and potential density (σ_θ, kg m^{-3}; dotted black isolines) over the South Scotia Ridge corresponding to day 28 from run I2K1. Section shown as black line at y = 300 in Figure 8a. For clarity purposes, Scotia Sea (SS), Weddell Sea (WS), and Weddell-Scotia Confluence (WSC) are marked at the sea surface. (d) Depth-averaged potential temperature anomaly (θ, °C) between day 28 and day 1 from run I2K1. Black contours show 1000, 2000, and 3000 m isobaths. Note different color ranges for Figures 8a and 8b. Note different orientations for Figures 8a and 8d ECCO2 cube-sphere projection, and Figure 8b CATS2008b stereographic projection.

Evolution of particle tracers that were injected into simulation H2K1 at two depths, above and below the shelf break (Figure 12) shows the presence of convergence areas along the continental shelf. Above the shelf break (Figure 12a), the particles show a V-shape. Below the shelf break (Figure 12b), they move downward toward the slope as seen in the realistic simulation with tides, RT (Figure 5a).

4. Discussion

Adding tides to our realistic model configuration of the WSC region improves the accuracy of the model solution relative to hydrographic and mooring data from the northern side of the South Scotia Ridge (SSR) in the southern Scotia Sea (see section 3.2). Idealized model configurations (section 3.3) demonstrate that the ASF and ASC can be explained through tide-driven processes.

### 4.1. Tide-Forced Mean Flows
Our homogeneous simulation H2K1 creates strong along-slope, depth-averaged, and daily-averaged currents (Figures 11c and 11d). When stratification is included (simulation I2K1), time-averaged downwelling at
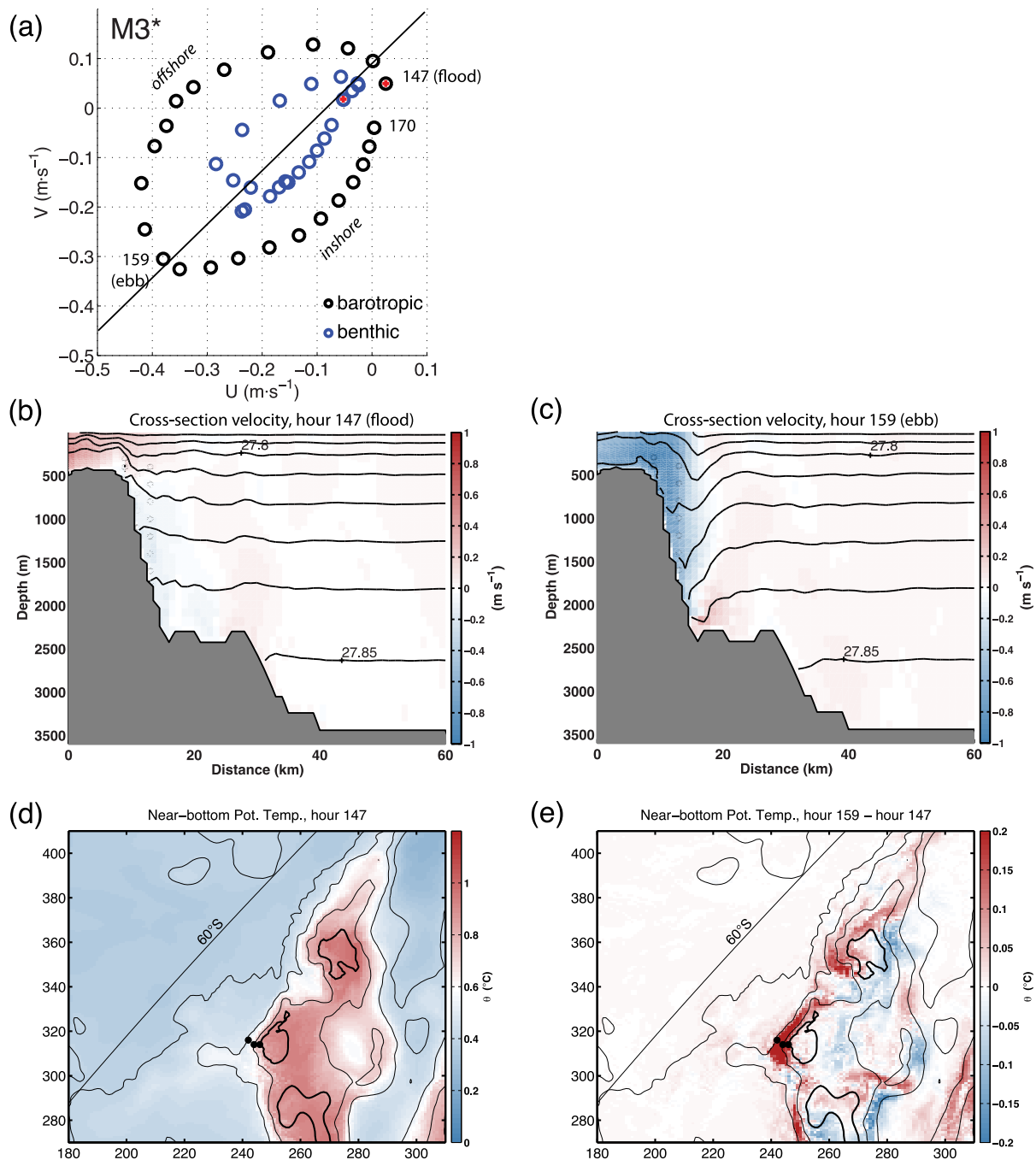
Figure 9. Idealized stratified ocean (experiment I2K1). (a) Hourly velocity during one K_1 tidal cycle for (black) depth-averaged barotropic field and (blue) near-bottom velocity at mooring M3*. Time series starts at hour 147 (flood; marked with a red cross), rotates counterclockwise and ends at hour 170. Diagonal black line indicates along-slope direction. (b, c) Vertical sections of velocity at (b) flood, hour 147 and (c) ebb, hour 159. (d) Near-bottom potential temperature (θ, °C) at flood. Contour lines show 500 (thick black line), 1000, 2000, and 3000 m isobaths. (e) Difference in near-bottom θ between flood and ebb (hour 159 minus hour 147).

the slope creates horizontal density gradients (Figure 9) that are qualitatively consistent with the observed structure of the ASF.

Barotropic cross-slope tidal currents can generate residual mean flows (averaged over an integral number of tidal cycles) through a variety of mechanisms [*Loder*, 1980; *Huthnance*, 1973, 1981] including friction, nonlinear interaction with background mean flows, and changes in tidal ellipse coefficients over a
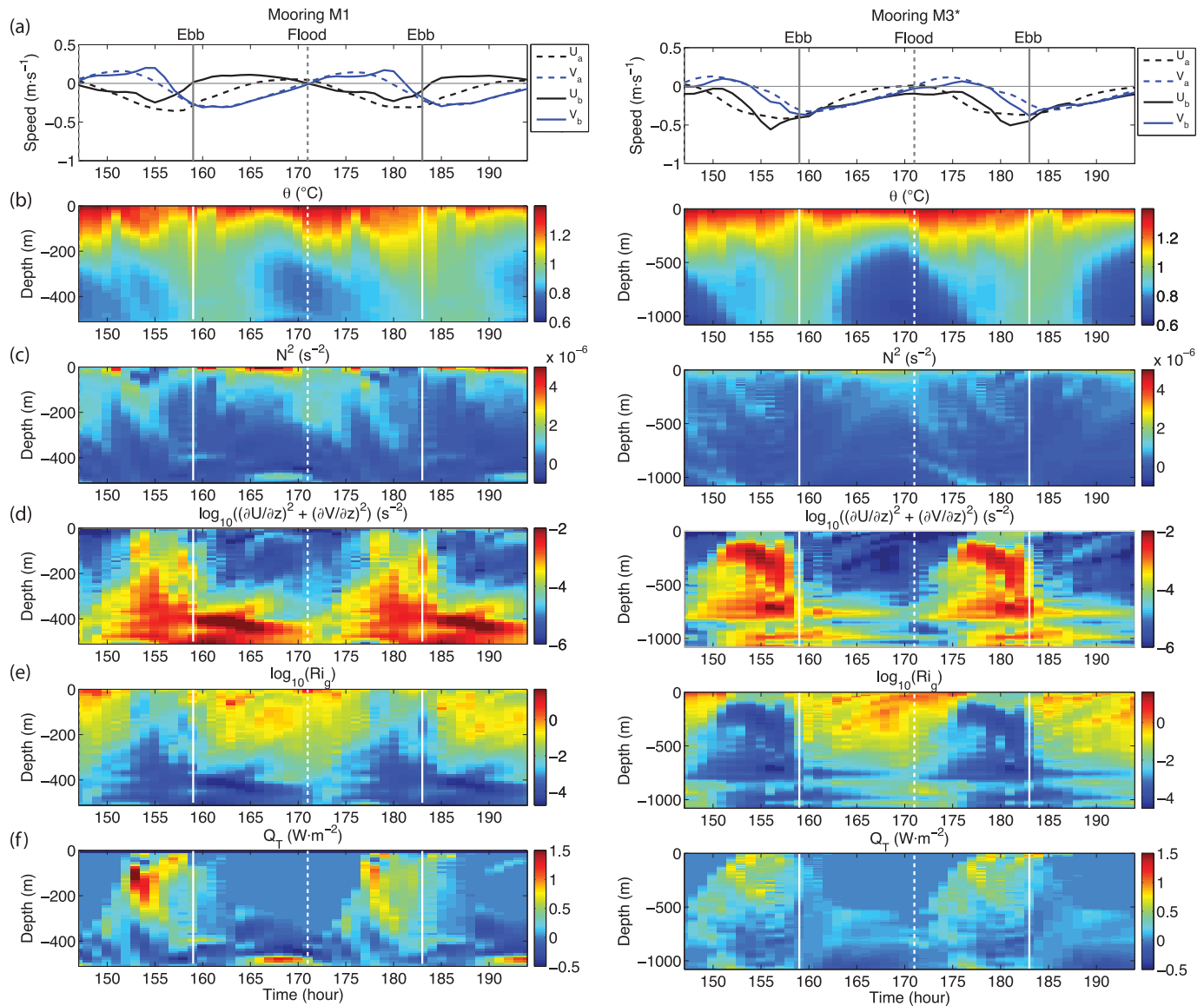
Figure 10. Idealized stratified ocean (experiment I2K1). Time series over two $2\times K_1$ tidal cycles at moorings M1 (left) and M3* (right). Vertical lines indicate flood (bold lines) and ebb (broken lines). (a) Velocity components (U and V, m s^{-1}) of depth-averaged velocity, "a," and near-bottom velocity, "b." (b) Potential temperature (θ, °C). (c) Stratification, as N^2 (s^{-2}), where N is the local buoyancy frequency. (d) Vertical velocity shear squared ($(\frac{\partial U}{\partial z})^2 + (\frac{\partial V}{\partial z})^2$, m s^{-2}). (e) Local gradient Richardson number, Ri_g. (f) Heat flux (Q_T, W m^{-2}), given by $Q_T = \rho C_p K_z (\frac{\partial T}{\partial z})$, where C_p is the specific heat ($C_p \sim 4 \cdot 10^3$ J kg^{-1}°C^{-1}).

typical tidal excursion by a water particle; for a graphic example of the latter, see Figure 10 in *Padman et al.* [2009]. Residual mean flows that can be measured at specific locations (e.g., at moorings) are called "Eulerian": these arise from volume continuity, friction, and the Coriolis force. Spatial variability of tidal current coefficients on scales comparable to or smaller than tide-driven advection during a tidal cycle introduces an additional residual circulation affecting freely-drifting particles; this component is called "Lagrangian." Equations (29) and (30) in *Loder* [1980] provide estimates of the Eulerian (v_E) and Lagrangian (v_L) residual currents based on deep-water cross-slope currents, water depth, bottom slope, tidal frequency, and f. Applying these values to the slope around the WSC, we estimate values of $\sim$0.01–0.1 m s^{-1} for both v_E and v_L. The higher values are associated with regions of large bottom slope, which is up to $\sim$0.3 close to our moorings. Values of v_E and v_L for the WSC region can be significant, but are smaller than the mean currents of 0.1–0.3 m s^{-1} produced by our homogeneous simulation H2K1 (Figures 11c and 11d).
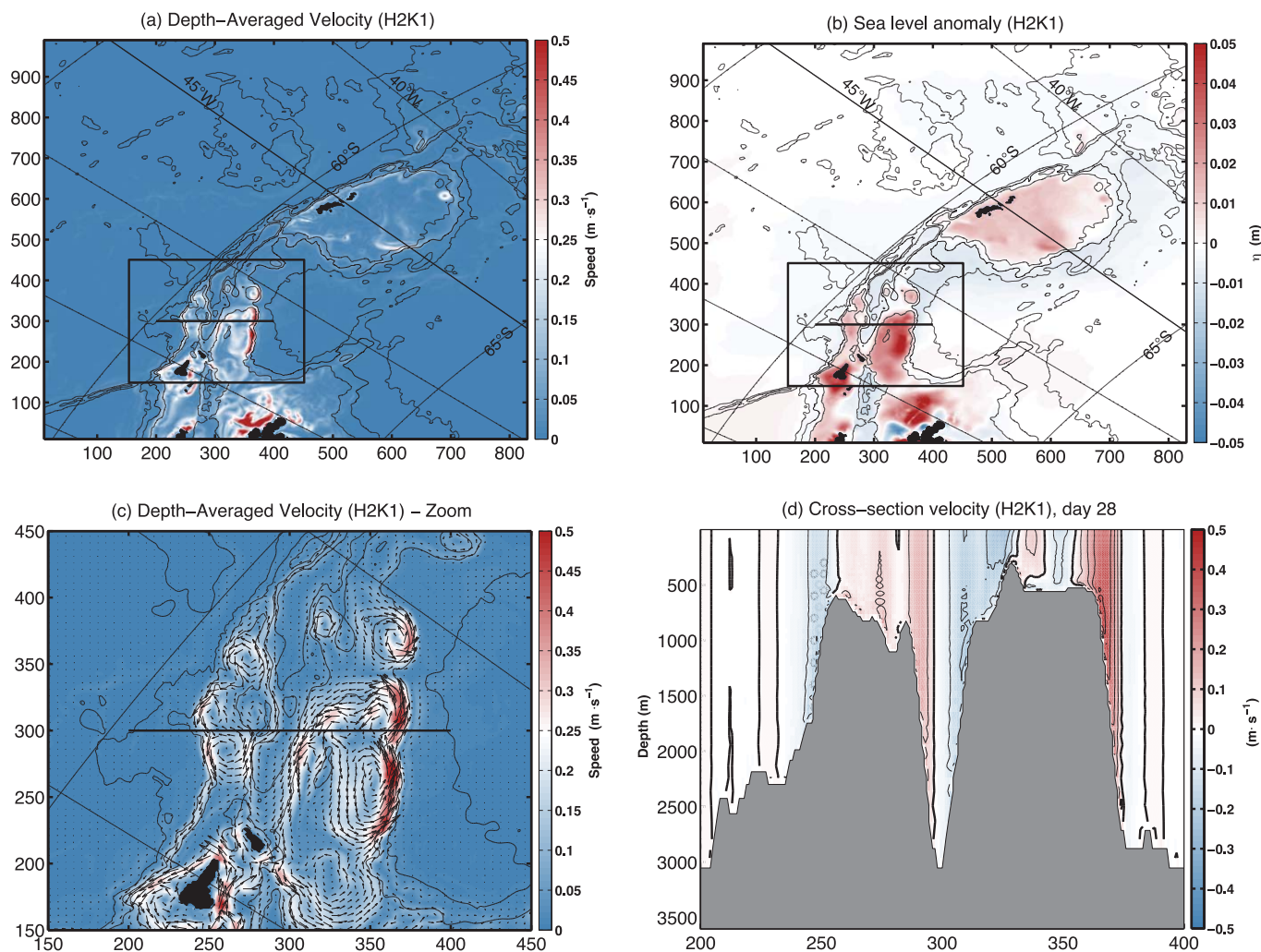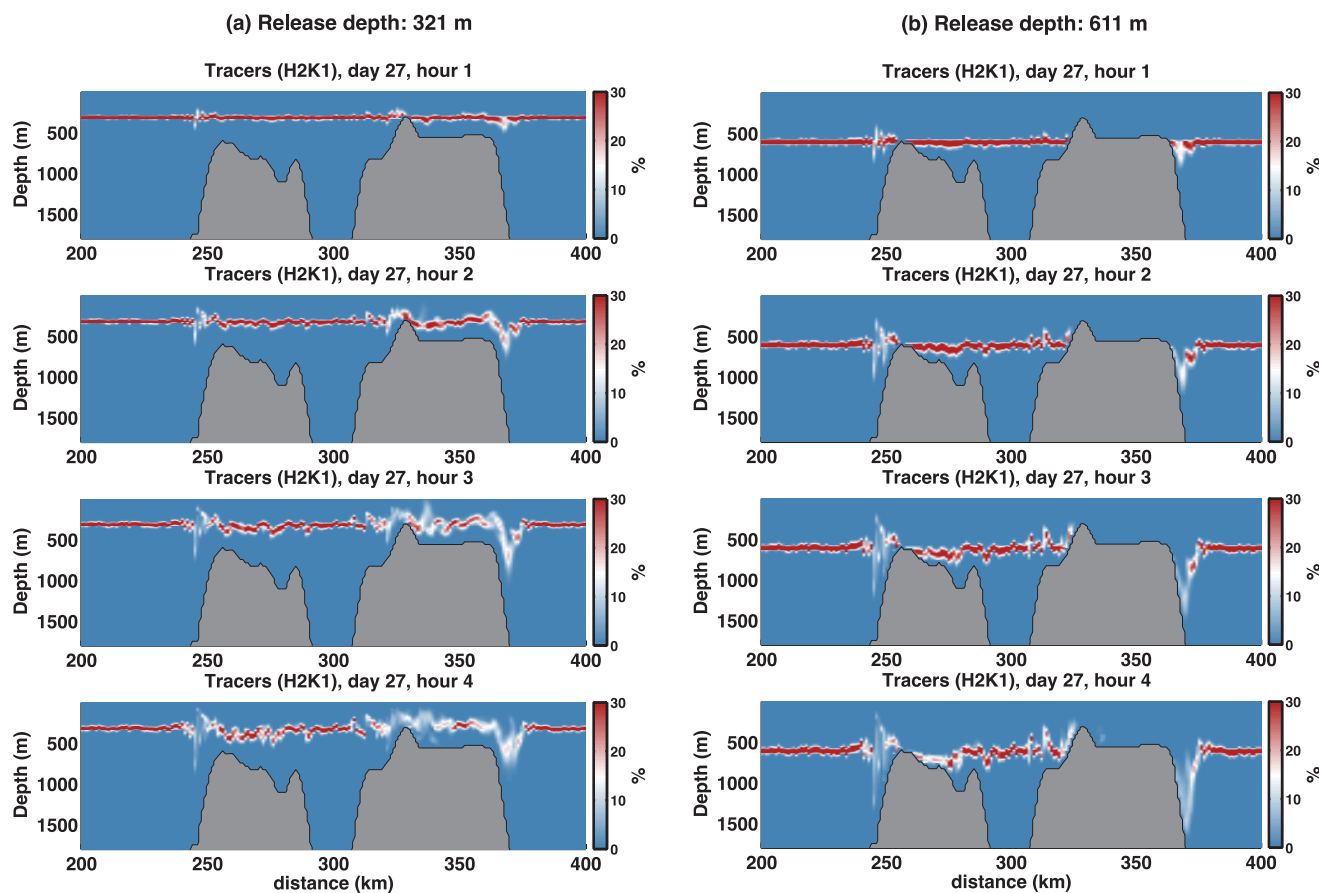
Figure 11. Homogeneous ocean (experiment H2K1). (a) Time mean (time averaged over 28 days) depth-averaged velocity (m s^{-1}). (b) Time mean (time averaged over 28 days) sea level anomaly (η, m). (c) Zoom of *a* over black box area shown in Figure 11a, with depth-averaged time mean velocity vectors. For clarity purposes, only 1:5 vectors are plotted. (d) Cross-section velocity (m s^{-1}, in color) over the South Scotia Ridge corresponding to day 28. Section shown as black line at y = 300 in Figures 11a–11c.

We attribute the large mean currents generated in H2K1 to the time-averaged accumulation of volume over the continental shelves and associated cross-slope surface pressure gradients at the shelf break and upper slope, as seen in the homogeneous simulation H2K1 (Figure 11b). This volume flux redistribution arises from spatial variability of Lagrangian residual mean circulation. In turn, this is caused by a combination of the tidal rectification mechanisms described by *Loder* [1980], vertical shear that is not included in the analytical solutions for v_E and v_L, and the two-dimensional structure of the real-world geometry of this region. For the WSC region, steady state occurs in a homogeneous ocean when the dynamic height over the continental shelf is ∼1–5 cm higher than over the deep ocean. Given ∼1–5 cm of surface pressure change over ∼10 km cross-slope distance, the expected barotropic geostrophic current is of ∼0.1–0.4 m s^{-1}, i.e., in agreement with the observed mean flow. Most of the volume brought into the WSC during model adjustment comes from Bransfield Strait and Powell Basin. At steady state, the dominant currents are parallel to isobaths; however, even when a quasi steady state geostrophic balance is reached, we expect ongoing cross-slope volume exchange driven by a net cross-slope flow in the bottom Ekman layer associated with the overlying along-isobath currents.

The preceding analysis describes how the ASC can be established by tides acting on a homogeneous ocean. In a more realistic stratified ocean, the flow will arrive at a balance described by the thermal wind relation.

(a) Release depth: 321 m
(b) Release depth: 611 m

Figure 12. Homogeneous ocean (experiment H2K1). Particle tracers released at day 27, hour 0, (a) at 321 m (i.e., above the shelf break), and (b) at 611 m (i.e., below the shelf break).

The isopycnal surfaces of the ocean interior adjust in response to the surface pressure gradient, deepening toward the continental slope. That is, advection can, in part, account for the mean vertical displacement of isopycnals observed in simulation I2K1 (Figure 7).

Ekman layer dynamics in the benthic layer also contribute to tilting of isopycnals over a slope [e.g., *Wåhlin et al.*, 2012; *Benthuysen et al.*, 2015]. Given an initial along-slope mean flow, regions of convergence and divergence arise from variations in the strength of the bottom Ekman layer, caused by variations in the geostrophic flow above the bottom boundary layer [*Benthuysen and Thomas*, 2013]. The convergence/divergence regions then act to tilt the isopycnals through the generation of vertical velocities sustaining, in turn, the geostrophic transport.

4.2. Mixing

Observations of enhanced vertical mixing associated with the interaction of tidal currents with steep or rough bathymetry are discussed by many authors [e.g., *Polzin et al.*, 1997; *Egbert and Ray*, 2000, 2001; *Tanaka et al.*, 2014; *Sprintall et al.*, 2014]. *Padman and Dillon* [1991] measured large tidal variability of diapycnal mixing rates over the Yermak Plateau in the eastern Arctic Ocean, in a setting comparable to the WSC region where most cross-slope tidal kinetic energy was associated with diurnal tides [*Padman et al.*, 1992]. *Polzin et al.* [1997] evaluated turbulent diffusivity during a period that included both spring and neap tides. Their microstructure data showed that mixing was enhanced throughout much of the water column in regions with rough topography, with values of 10^{-3} m^2 s^{-1} within 150 m of the bottom, values larger than 10^{-4} m^2 s^{-1} within 300 m of the bottom, and values larger than 10^{-5} m^2 s^{-1} higher in the water column (their Figure 3). Motivated by these studies, we expect the WSC region to experience substantial tide-

induced mixing, with modulation both at the fundamental frequency of the tide ($\sim$1 cpd) and over the spring/neap cycle ($\sim$0.07 cpd, or $\sim$14 day period).

Tidal contributions to mixing in the WSC region can occur at lateral and bottom boundaries [*Patterson and Sievers*, 1980; *Naveira Garabato et al.*, 2004], and within the stratified ocean interior [*Naveira Garabato et al.*, 2007] through generation of baroclinic tides at the seabed followed by vertical radiation of these internal waves [*Padman et al.*, 2006]. Additional mixing may occur at the base of the ice pack, when present, if the ice is not in free drift [*Padman et al.*, 1992]. The combination of tide-modulated stratification (N^2; Figure 10c) and intensified velocity shear (Figure 10d) in our idealized stratified simulation I2K1 results in tidal-period variability of gradient Richardson number Ri_g (Figure 10e). In the KPP mixing scheme used by MITgcm to calculate diapycnal diffusivity and viscosity (K_z and A_z), Ri_g is the fundamental control on mixing in the stratified ocean below the surface boundary layer, with values of $Ri_g < 1$ indicating energetic turbulence. Low values of Ri_g occur throughout most of the water column.

Regions of low Ri_g (implying high A_z) close to the seabed imply momentum loss through friction, with tidal modulation indicating the process by which the oscillatory flow can lead to rectified mean circulation. Water mass transformation by diapycnal mixing requires not only high values of K_z but also significant vertical gradients of the stratifying scalar(s) being mixed. In simulation I2K1, the stratifying scalar is $\theta(z)$, and diapycnal mixing can be represented by the associated heat flux Q_T (Figure 10f). These values, of order 1 W m^{-2} in simulation I2K1 at the locations of our moorings, are quite small relative to fluxes in some other tide-dominated regions. For example, *Padman and Dillon* [1991] reported $\sim$25 W m^{-2} over the edge of the Yermak Plateau in the eastern Arctic Ocean. However, I2K1 stratification is weak relative to the more realistic WSC (compare density ranges in Figure 5 (RT) and Figure 7 (I2K1)), and very weak relative to the Arctic study of *Padman and Dillon* [1991]. Larger vertical gradients of $\theta(z)$ will lead to larger Q_T which could increase the contribution of diapycnal mixing in the WSC region.

4.3. The Antarctic Slope Front and Current in the Scotia Sea Sector

Tide-induced mean circulation and mixing appear, from our idealized model studies discussed in the preceding sections, to be sufficiently energetic to impact the overall hydrography and circulation in the WSC region. Our recent observations show the ASF (Figure 2b) and the associated westward-flowing ASC (Table 2) on the northern side of the South Scotia Ridge (SSR), the latter being consistent with earlier studies [*Nowlin and Zenk*, 1988; *Palmer et al.*, 2012]. Our realistic simulation with atmospheric forcing but without tides (RnoT) reproduces the ASC around the edge of Powell Basin (Figure 6b), but the modeled flow in the Scotia Sea sector is strongly dominated by the ACC fronts and no ASF is generated there (Figure 2h). This result is in agreement with the recent high-resolution numerical model of *Jiang et al.* [2013], also run without tides. However, when tides are added (simulation RT), the ASF and ASC are generated at the mooring site (Figure 2e and Table 2). Time-averaged and depth-averaged currents throughout the model domain are, in most locations, increased by adding tides, especially along the continental slopes (Figure 6). Adding tides also improves the accuracy of modeled seasonal variability of hydrographic properties (Figure 3). In particular, seasonal minimum values of $\theta(S)$ at the moorings in August–September are well reproduced. Adding tides generates the fortnightly *Mf* tide seen in measurements (Figure 4, Tables 3 and 5).

Our idealized homogeneous simulation with tide forcing only (H2K1) generates time-averaged barotropic tidal current speeds (Figure 11a) that are comparable to those in the CATS2008b forcing model (Figure 8b). The spatial structure of these current speeds, combined with nonlinear bottom friction, leads to spatially-varying mean flows that advect water laterally (Figure 11) and vertically (Figure 12). Convergence and divergence of these mean flows establishes a balance with surface pressure gradients (Figure 11b) as the dynamic height increases over the continental shelf regions occupied, in the real world, by the WSC. In this model configuration, tidally induced time mean currents on the northern side of the SSR near our moorings are $\sim$0.1–0.2 m s^{-1} (Figures 11c and 11d). Therefore, neither atmospheric forcing nor stratification is necessary to generate the ASC near our moorings.

When idealized stratification is added (simulation I2K1), isopycnals below the depth of the shelf break are deflected downward toward the continental slope (Figures 7b and 8c), consistent with observations (Figure 2b). The modeled along-slope mean current near our moorings in I2K1 is increased relative to the homogeneous run (H2K1) (compare Figure 8c with Figure 11d). The currents in I2K1 are comparable to measured values and to those in the fully forced, realistic simulation RT (see Figure 5).

These results demonstrate that both spatially varying tide-forced mean advection and stratification are important processes contributing to the ASF and ASC in this region. Enhancement of mixing by tides (Figure 10) may also play a role. While it is impossible to fully separate the roles of advection, stratification and mixing in establishing the ASF and ASC in this region, a plausible scenario is as follows. First, tides establish a mean surface pressure gradient field through convergent and divergent flows determined by variability in tidal coefficients, nonlinear (quadratic) bottom friction, and vertical shear. Second, subsurface downwelling over the continental slope (Figure 12) associated with the barotropic mean circulation develops the cross-slope density gradients to create the ASF, further intensifying the along-slope flow (ASC) and friction at the seabed. Mixing, with rates that are highly variable in space, then consolidates the along-slope current (ASC).

This process for creating the ASF and ASC does not require any input from atmospheric forcing, and therefore would suggest that, in this region, tides may be the dominant cause of the ASF and ASC, in contrast to previous studies that have focused on the response of the ocean to spatial patterns of wind (e.g., *Deacon* [1937] and *Sverdrup* [1953], as cited by *Gill* [1973]). More recent sensitivity experiments to atmospheric forcing fields have suggested that the along-slope wind speed controls the water mass transport and the seasonal cycle of the ASC [*Mathiot et al.*, 2011]. The idealized modeling study of *Stewart and Thompson* [2012] indicated that the zonal wind stress could explain the presence of a single-sided slope front, with a V-shaped front resulting from the inclusion of outflows of dense water formed on the continental shelf. These authors suggested that the export of bottom water and the deep overturning circulation is more sensitive to easterlies blowing over the Antarctic continental shelf than to the polar westerlies blowing over the ACC. North of the Antarctic Peninsula, however, westerlies are the dominant winds [e.g., *Beckmann et al.*, 1999], and the complex bathymetry implies that the angle between the continental slope and the prevailing wind stress varies over short distances. The absence of a dominant along-slope wind stress direction relative to isobath alignment may explain why tidal currents have a prominent role in forcing along-slope flows around the WSC.

4.4. Weddell-Scotia Confluence

The addition of tidal forcing to our model also improves our representation of the different water mass properties of the WSC. With tides, our model simulates the spatial variability of AASW and MCDW seen in CTD transects across the continental slope (Figure 2). The spatial density gradients over the WSC are modified, showing more homogeneous characteristics over the WSC than in the open oceans north and south of the WSC (noted as *SS* and *WS* in Figure 8c). These results confirm that tides not only affect the structure of the ASF and the strength of the ASC, but also the larger-scale characteristics of the WSC.

4.5. Fortnightly Variability

The inclusion of tides in our realistic model configuration provides substantial improvements in comparisons with time-averaged currents at our moorings. Including tides also improves model representation of low-frequency ($f < 0.5$ cpd) variability of currents (Figure 4b), providing added confidence that our model is correctly representing tidal effects including interactions with circulation driven by other forcings. In particular, simulation RT almost exactly reproduces the measured strong narrowband signal at frequency $f \approx 0.07$ cpd (Figure 4) that is interpreted by our tidal analyses with "T_TIDE" as the *Mf* tide (period of $\sim$13.66 days). The semimajor axis current for this tidal constituent ($U_{maj}(Mf)$) has values of $\sim$0.01–0.06 m s^{-1} (Tables 2 and 5), which are similar to those for the fundamental tidal harmonics at $\sim$1 and $\sim$2 cpd (Tables 3 and 4). Comparable results were also reported from measurements along the Ross Sea continental slope by *Budillon et al.* [2011]. We hypothesize that the *Mf* tide provides insight to the processes by which the modeled tidal forcing (at $\sim$1 and $\sim$2 cpd) ultimately contributes to changes in mean flows.

In global models, the *Mf* tide is the largest of the zonally symmetric, long-period tides, and arises from the time-varying modulation of the Earth's permanent tide M_0 caused by changes in the Moon's declination [*Cartwright and Ray*, 1990; *Ray and Egbert*, 2012]. Typical currents associated with the *Mf* tide are, however, only of order 10^{-3} m s^{-1} [*Egbert and Ray*, 2003; *Ray and Egbert*, 2012], about 1–2 orders of magnitude lower than we measured at our moorings. Therefore, we seek explanations for how these large measured *Mf* currents can arise.

The *Mf* period corresponds to the beat period of the energetic K_1 and O_1 diurnal tidal components (Table 4), the components with the largest currents in the WSC region. Therefore, interactions between K_1 and O_1 might play a role in providing a large $\sim$2 week periodicity. Two potential mechanisms are as follows. First,

since bottom friction is nonlinear with current speed, it is possible that the much higher daily averaged benthic friction at spring tide (K_1 and O_1 in phase) reduces the currents for individual tidal harmonics at that time relative to their long-term average including neap tide periods. Second, in the presence of an existing narrow but energetic along-slope current, variability of the cross-slope location of the mean current by processes varying with the spring/neap modulation may appear as an apparently strong Mf-period current in a tidal analysis from a mooring. For example, if the mean current is $\sim$0.2 m s^{-1} and is offshore from a mooring for $\sim$7 days around spring tide but captured by the mooring for $\sim$7 days around neap tide, over one spring/neap cycle a current meter on the mooring may record a mean flow of about 0.1 m s^{-1} and an Mf tide with $U_{maj}(Mf)$ $\sim$0.1 m s^{-1}, with the ellipse oriented along-slope.

The mean along-slope current near $z = 600$ m at moorings M1 and M2 are $\sim$0.25 m s^{-1} and $\sim$0.10 m s^{-1}, respectively (Table 2). Obtaining an along-slope Mf current with amplitude of $\sim$0.05 m s^{-1} (Table 5) would require cross-slope advection of the narrow current, on Mf time scales, of a similar distance to the separation of these moorings, $\sim$4 km. Since the flow consists of both a barotropic (Figure 11) and baroclinic component (Figure 5, and Figures 7–9), offshore motion of the ASC may be driven by changes in either tidal rectification or cross-slope motion of the subsurface density front (the ASF).

5. Conclusions

Recent measurements from the northern side of the South Scotia Ridge in the southern Scotia Sea provide valuable information on the structure and time-dependent behavior of the Antarctic Slope Front (ASF) and the associated westward-flowing Antarctic Slope Current (ASC) in this region. Current meter time series near the shelf break and over the continental slope are dominated by tides, with the strongest constituents being the primary diurnal tides K_1 and O_1 with semimajor ellipse axes (U_{maj}) of $\sim$0.05–0.15 m s^{-1}. Current meter time series also contain a large amplitude fortnightly Mf tide (period $\sim$13.66 days), with $U_{maj}(Mf)$ almost always in the range $\sim$0.03–0.06 m s^{-1} and the major axis directed along-slope.

These measurements, and previous studies of the ASF in the Ross Sea, suggest that tides may contribute to forming the ASF and ASC and determining mixing and cross-slope transport of shelf-resident waters toward the deep ocean. We investigated the role of tides in the Weddell-Scotia Confluence (WSC) region using a suite of high-resolution numerical simulations (lateral grid-spacing of $\sim$1 km and 80 vertical levels) of varying complexity. Comparing two realistic atmospherically forced simulations, without and with tides, shows that tidal forcing is required to capture key features of the regional hydrography including: cross-slope gradient of surface potential density σ_θ; downward tilting of subsurface isopycnals toward the continental slope; the vertical density structure in the WSC; and the seasonal variability of (θ, S) properties of Modified Circumpolar Deep Water (MCDW). The simulation with tides also captures the energy of the fortnightly Mf tide, even though the only tide components in the forcing fields have diurnal ($\sim$1 cpd) and semidiurnal ($\sim$2 cpd) frequencies. Adding tides increases the mean flow of the ASC in the vicinity of the moorings and elsewhere in the WSC region.

Idealized simulations, forced only with tides and simplified initial hydrographic fields, demonstrate that the ASF and ASC can be generated in the WSC region without any atmospheric forcing. Two processes are responsible: development of strong cross-slope pressure gradients by volume redistribution associated with spatial variations in Lagrangian residual mean circulation (section 4.1); and mixing at the seabed and throughout the water column, enhanced by periodic (tidal) cross-slope advection that brings deep water from offshore up to the outer continental shelf (section 4.2). These simulations also confirm that tidal processes can contribute to the large-scale distribution of water mass properties over the continental shelf within the WSC.

We conclude that processes associated with tides are sufficient to explain the basic frontal structures and mean circulation in the WSC region. Tidal effects must, therefore, be included in climate models that attempt to reproduce the larger-scale circulation and hydrography along the margins of the Scotia Sea, and the contribution of Weddell Sea water masses to the global ocean. These effects include the downstream modification of Southern Ocean water mass properties east of Drake Passage due to intrusions of intermediate waters derived from the WSC, and injection of Antarctic Bottom Water into the subpolar ocean from its source regions around the Antarctic continent.

Even in our $\sim$1 km model configurations, some relevant processes are not well resolved. The extreme bathymetric slope in places along the South Scotia Ridge — up to $\sim$0.3 in the region of our moorings — implies

that even higher resolution may be required to capture the full effects of the complex bathymetry. Given that bathymetry in this region is not fully mapped at the needed resolution, errors will remain in models even if grid resolution could be further increased. The dominant tidal constituents in currents in this region are diurnal; these constituents can be difficult to model accurately because of their dependence on small-scale topography, mean along-slope flows, and stratification [*Padman et al.*, 1992; *Skarðhamar et al.*, 2015]. Mixing above the benthic boundary layer depends on the generation of baroclinic tides and higher wave-number internal gravity waves, which are not fully resolved in our grid. The interaction of these baroclinic waves with the sea-ice cover may influence the seasonal variability of the open-water (lead) fraction in this region [*Padman et al.*, 2006] which could then contribute to the formation and melting of the sea-ice pack and the consequent modification of surface mixed layer stability [*Koentopp et al.*, 2005].

Finally, we note that many of the tidal effects described above can only be generated in a model that has a much finer grid that those of existing coupled climate models (CCMs). Simply adding tides to CCMs will not necessarily reproduce the tidal effects reported here. Thus, there is a need to develop parameterizations of tidal effects for inclusion in CCMs, which is relatively simple for diffusive and viscous effects but more complicated for advective processes.

References

Adcroft, A., C. Hill, and J. A. Marshall (1997), Representation of topography by shaved cells in a height coordinate ocean model, *Mon. Weather Rev.*, *125*, 2293–2315.

Adcroft, A., J. Campin, C. Hill, and J. Marshall (2004), Implementation of an atmosphere-ocean general circulation model on the expanded spherical cube, *Mon. Weather Rev.*, *132*, 2845–2863.

Ainley, D. G., and S. S. Jacobs (1981), Sea-bird affinities for ocean and ice boundaries in the Antarctic, *Deep Sea Res., Part A*, *28*, 1173–1185.

Arndt, J. E., et al. (2013), The International Bathymetric Chart of the Southern Ocean (IBCSO) Version 1.0: A new bathymetric compilation covering circum-antarctic waters, *Geophys. Res. Lett.*, *40*, 3111–3117, doi:10.1002/grl.50413.

Beckmann, A., H. H. Hellmer, and R. Timmermann (1999), A numerical model of the Weddell Sea: Large-scale circulation and water mass distribution, *J. Geophys. Res.*, *104*, 23,375–23,391.

Benthuysen, J., and L. Thomas (2013), Nonlinear stratified spindown over a slope, *J. Fluid Mech.*, *726*, 371–403.

Benthuysen, J., L. Thomas, and S. Lentz (2015), Rapid generation of upwelling at a shelf break caused by buoyancy shutdown, *J. Phys. Oceanogr.*, *45*, 294–312.

Budillon, G., P. Castagno, S. Aliani, G. Spezie, and L. Padman (2011), Thermohaline variability and Antarctic Bottom Water formation at the Ross Sea shelf break, *Deep Sea Res., Part I*, *58*, 1002–1018.

Carmack, E. C., and P. D. Killworth (1978), Formation and interleaving of abyssal water masses off Wilkes Land, Antarctica, *Deep Sea Res.*, *25*, 357–369.

Cartwright, D. E., and R. D. Ray (1990), Observations of the *Mf* ocean tide from GEOSAT altimetry, *Geophys. Res. Lett.*, *17*, 619–622.

Caspel, M., M. Schroeder, O. Huhn, and H. H. Hellmer (2015), Precursors of Antarctic Bottom Water formed on the continental shelf off Larsen Ice Shelf, *Deep Sea Res., Part I*, *99*, 1–9.

Daru, V., and C. Tenaud (2004), High order one-step monotonicity-preserving schemes for unsteady compressible flow calculations, *J. Comput. Phys.*, *193*, 563–594.

Deacon, G. E. R. (1937), The hydrology of the Southern Ocean, *Discovery Reports*, *15*, 1–24.

Egbert, G. D., and R. D. Ray (2000), Significant dissipation of tidal energy in the deep ocean inferred from satellite altimeter data, *Nature*, *405*, 775–778.

Egbert, G. D., and R. D. Ray (2001), Estimates of M2 tidal dissipation from TOPEX/Poseidon altimeter data, *J. Geophys. Res.*, *106*, 22,475–22,502.

Egbert, G. D., and R. D. Ray (2003), Deviation of long-period tides from equilibrium: Kinematics and geostrophy, *J. Phys. Oceanogr.*, *33*, 822–839.

Fahrbach, E., G. Rohardt, N. Scheele, M. Schroeder, V. Strass, and A. Wisotzki (1995), Formation and discharge of deep and bottom water in the north western Weddell Sea, *J. Mar. Res.*, *53*, 515–538.

Foreman, M. G. G. (1978), Manual for tidal currents analysis and prediction, Pacific Marine Science Report., 78-6, 57 pp., Inst. of Ocean Sci., Patricia Bay, Sidney, B. C.

Foster, T. D., and E. C. Carmack (1976a), Frontal zone mixing and Antarctic Bottom Water formation in the southern Weddell Sea, *Deep Sea Res.*, *23*, 301–317.

Foster, T. D., and E. C. Carmack (1976b), Temperature and salinity structure in the Weddell Sea, *J. Phys. Oceanogr.*, *6*, 36–44.

Fox-Kemper, B., and D. Menemenlis (2008), Can large eddy simulation techniques improve mesoscale rich ocean models?, in *Ocean Modeling in an Eddying Regime*, edited by M. Hecht and H. Hasumi, pp. 319–338, AGU, Washington, D. C.

Gill, A. E. (1973), Circulation and bottom water production in the Weddell Sea, *Deep Sea Res. Oceanogr. Abstr.*, *20*, 111–140.

Gordon, A. L. (1967), Structure of Antarctic waters between 20°W and 170°W, in *Antarct. Map Folio Series, Folio. 6*, edited by V. C. Bushnell, 10 pp., Am. Geogr. Soc.

Gordon, A. L., E. Zambianchi, A. H. Orsi, M. Visbeck, C. F. Guilivi, T. Whitworth III, and G. Spezie (2004), Energetic plumes over the western Ross Sea continental slope, *Geophys. Res. Lett.*, *31*, L21302, doi:10.1029/2004GL020785.

Gordon, A. L., A. H. Orsi, R. Muench, B. A. Huber, E. Zambianchi, and M. Visbeck (2009), Western Ross Sea continental slope gravity currents, *Deep Sea Res., Part II*, *13–14*, 796–817.

Hellmer, H., M. Schroeder, C. Haas, G. Dieckmann, and M. Spindler (2008), The ISPOL drift experiment, *Deep Sea Res., Part II*, *55*, 913–917.

Heywood, K. J., A. C. Naveira Garabato, D. P. Stevens, and R. D. Muench (2004), On the fate of the Antarctic Slope Front and the origin of the Weddell Front, *J. Geophys. Res.*, *109*, C06021, doi:10.1029/2003JC002053.

Huthnance, J. M. (1973), Tidal current asymmetries over the Nor folk Sandbanks, *Estuarine Coastal Mar. Sci.*, *1*, 89–99.

Huthnance, J. M. (1981), On mass transports generated by tides and long waves, *J. Fluid Mech.*, *102*, 367–387.

Jackett, D. R., and T. J. McDougall (1995), Minimal adjustment of hydrographic data to achieve static stability, *J. Atmos. Oceanic Technol.*, *12*, 381–389.

Jacobs, S. S. (1991), On the nature and significance of the Antarctic Slope Front, *Mar. Chem.*, *35*, 9–24.

Jiang, M., M. A. Charette, C. I. Measures, Y. Zhu, and M. Zhou (2013), Seasonal cycle of circulation in the Antarctic Peninsula and the off-shelf transport of shelf waters into southern Drake Passage and Scotia Sea, *Deep Sea Res., Part II*, *90*, 15–30.

Killworth, P. D. (1977), Mixing on the Weddell Sea continental slope, *Deep Sea Res.*, *24*, 427–448.

Koentopp, M., O. Eisen, C. Kottmeier, L. Padman, and P. Lemke (2005), Influence of tides on sea ice in the Weddell Sea: Investigations with a high-resolution dynamic-thermodynamic sea ice model, *J. Geophys. Res.*, *110*, C02014, doi:10.1029/2004JC002405.

Large, W. G., J. C. McWilliams, and S. C. Doney (1994), Oceanic vertical mixing: A review and a model with a nonlocal boundary layer parameterization, *Rev. Geophys.*, *32*, 363–403.

Loder, J. W. (1980), Topographic rectification of tidal currents on the sides of Georges Bank, *J. Phys. Oceanogr.*, *10*, 1399–1416.

Losch, M., D. Menemenlis, J.-M. Campin, P. Heimback, and C. Hill (2010), On the formulation of sea-ice models. Part 1: Effects of different solver implementations and parameterizations, *Ocean Modell.*, *33*, 129–144.

Marshall, J. A., A. Adcroft, C. Hill, L. Perelman, and C. Heisey (1997), A finite-volume, incompressible Navier-Stokes model for studies of the ocean on parallel computers, *J. Geophys. Res.*, *102*, 5753–5766.

Mathiot, P., H. Goosse, T. Fichefet, B. Barnier, and H. Gallee (2011), Modelling the seasonal variability of the Antarctic Slope Current, *Ocean Sci.*, *7*, 455–470.

Menemenlis, D., J. Campin, P. Heimbach, C. Hill, T. Lee, A. Nguyen, M. Schodlok, and H. Zhang (2008), ECCO2: High resolution global ocean and sea ice data synthesis, *Mercator Ocean Quart. Newsl.*, *31*, 13–21.

Muench, R. D., L. Padman, A. L. Gordon, and A. H. Orsi (2009), A dense water outflow from the Ross Sea, Antarctica: Mixing and the contribution of tides, *J. Mar. Syst.*, *77*, 369–387.

Naveira Garabato, A. C., K. L. Polzin, B. A. King, K. J. Heywood, and M. Visbeck (2004), Widespread intense turbulent mixing in the Southern Ocean, *Science*, *303*, 210–213.

Naveira Garabato, A. C., D. P. Stevens, A. J. Watson, and W. Roether (2007), Short-circuiting of the overturning circulation in the Antarctic Circumpolar Current, *Nature*, *447*, 194–197.

Nowlin, W. D., Jr., and W. Zenk (1988), Westward bottom currents along the margin of the South Shetland Island Arc, *Deep Sea Res., Part A*, *35*, 269–301.

Orsi, A. H., and C. Wiederwohl (2009), A recount of Ross Sea waters, *Deep Sea Res., Part II*, *56*, 778–795.

Orsi, A. H., W. Smethie, and J. L. Bullister (2002), On the total input of Antarctic waters to the deep ocean: A preliminary estimate from chlorofluorocarbon measurements, *J. Geophys. Res.*, *107*(C8), 3122, doi:10.1029/2001JC000976.

Padman, L., and T. M. Dillon (1991), Turbulent mixing near the Yermak Plateau during the Coordinated Eastern Arctic Experiment, *J. Geophys. Res.*, *96*, 4769–4782.

Padman, L., A. Plueddemann, R. D. Muench, and R. Pinkel (1992), Diurnal tides near the Yermak Plateau, *J. Geophys. Res.*, *97*, 12,639–12,652.

Padman, L., H. A. Fricker, R. Coleman, S. Howard, and L. Erofeeva (2002), A new tidal model for the Antarctic ice shelves and seas, *Ann. Glaciol.*, *34*, 247–254.

Padman, L., S. L. Howard, and R. D. Muench (2006), Internal tide generation along the South Scotia Ridge, *Deep Sea Res., Part II*, *53*, 157–171.

Padman, L., S. L. Howard, A. H. Orsi, and R. D. Muench (2009), Tides of the Northwestern Ross Sea and their impact on dense outflows of Antarctic Bottom Water, *Deep Sea Res., Part II*, *56*, 818–834.

Palmer, M. (2012), Outflow of Weddell Sea waters into the Scotia Sea through the western sector of the South Scotia Ridge, PhD thesis, 146 pp., Univ. of the Balearic Islands, Spain.

Palmer, M., D. Gomis, M. M. Flexas, G. Jorda, L. Juillon, T. Tsubouchi, and A. Naveira Garabato (2012), Water mass pathways and transports over the South Scotia Ridge west of 50°W, *Deep Sea Res., Part I*, *59*, 8–24.

Patterson, S. L., and H. A. Sievers (1980), The Weddell-Scotia Confluence, *J. Phys. Oceanogr.*, *10*, 1584–1610.

Pawlowicz, R., B. Beardsley, and S. Lentz (2002), Classical tidal harmonic analysis including error estimates in MATLAB using T_TIDE, *Comput. Geosci.*, *28*, 929–937.

Polzin, K. L., J. M. Toole, J. Ledwell, and R. Schmitt (1997), Spatial variability of turbulent mixing in the abyssal ocean, *Science*, *276*, 93–96.

Ray, R. D., and G. D. Egbert (2012), Fortnightly Earth rotation, ocean tides, and mantle anelasticity, *Geophys. J. Int.*, *189*, 400–413.

Simmons, A., S. Uppala, D. Dee, and S. Kobayashi (2007), The ERA interim reanalysis, in *ECMWF Newsletter*, vol. 110, pp. 25–35, ECMWF, Reading, U. K.

Skarðhamar, J., Ø. Skagseth, and J. Albretsen (2015), Diurnal tides on the Barents sea continental slope, *Deep Sea Res., Part I*, *97*, 40–51.

Smith, W. H. F., and D. T. Sandwell (1997), Global seafloor topography from satellite altimetry and ship depth soundings, *Science*, *277*, 1957–1962.

Sprintall, J., A. L. Gordon, A. Koch-Larrouy, T. Lee, J. T. Potemra, K. Pujiana, and S. E. Wijffels (2014), The Indonesian seas and their role in the coupled ocean-climate system, *Nat. Geosci.*, *7*, 487–492.

Stewart, A. L., and A. F. Thompson (2012), Sensitivity of the oceans deep overturning circulation to easterly Antarctic winds, *Geophys. Res. Lett.*, *39*, L18604, doi:10.1029/2012GL053099.

Sverdrup, H. U. (1953), The currents off the coast of Queen Maud Land, *Norsk Geogr. Tidsskr.*, *14*, 239–249.

Tanaka, Y., I. Yasuda, S. Osafune, T. Tanaka, J. Nishioka, and Y. N. Volkov (2014), Internal tides and turbulent mixing in the Bussol Strait, *Progr. Oceanogr.*, *126*, 98–108.

Thompson, A. F., and K. J. Heywood (2008), Frontal structure and transport in the northwestern Weddell Sea, *Deep Sea Res., Part I*, *55*, 1229–1251.

Thompson, A. F., K. J. Heywood, S. Schmidtko, and A. L. Stewart (2014), Eddy transport as a key component of the Antarctic overturning circulation, *Nat. Geosci.*, *7*, 879–884, doi:10.1038/ngeo2289.

Trasviña, A., K. Heywood, A. H. H. Renner, S. E. Thorpe, A. F. Thompson, and L. Zamudio (2011), The impact of high-frequency current variability on dispersion off the eastern Antarctic Peninsula, *J. Geophys. Res.*, *116*, C11024, doi:10.1029/2011JC007003.

Wåhlin, A. K., R. D. Muench, L. Arneborg, G. Björk, and H. Alsén (2012), Some implications of Ekman layer dynamics for cross-shelf exchange in the Amundsen Sea, *J. Phys. Oceanogr.*, *42*, 1461–1474.

Wang, Q., S. Danilov, H. Hellmer, and J. Schröter (2010), Overflow dynamics and bottom water formation in the western Ross Sea: Influence of tides, *J. Geophys. Res.*, *115*, C10054, doi:10.1029/2010JC006189.

Whitworth, T. III, and A. H. Orsi (2006), Antarctic Bottom Water production and export by tides in the Ross Sea, *Geophys. Res. Lett.*, *33*, L12609, doi:10.1029/2006GL026357.

Whitworth, T. III, W. D. Nowlin Jr., A. H. Orsi, R. A. Locarnini, and S. G. Smith (1994), Weddell Sea Shelf Water in the Bransfield Strait and Weddell-Scotia Confluence, *Deep Sea Res., Part I*, *41*, 629–641.

Whitworth, T. III, A. H. Orsi, S. J. Kim, and W. D. Nowlin Jr. (1998), Water masses and mixing near the Antarctic Slope Front, in *Ice, and Atmosphere: Interactions at the Antarctic Continental Margin, Antarctic Res. Ser.*, vol. 75, edited by S. S. Jacobs and R. F. Weiss, pp. 1–27, AGU, Washington, D. C.